

Recent Progress of Promising Cathode Candidates for Sodium-Ion Batteries: Current Issues, Strategy, Challenge, and Prospects

Chenxi Peng, Xijun Xu,* Fangkun Li, Lei Xi, Jun Zeng, Xin Song, Xuanhong Wan, Jingwei Zhao,* and Jun Liu*

Lithium-ion batteries (LIBs) have dominated the secondary batteries market in the past few decades. However, their widespread application is seriously hampered by the limited lithium resource and high cost. Recently, sodium-ion batteries (SIBs) have generated significant attention because of their characteristics of abundant raw sources, low cost, and similar “rocking chair” mechanism with LIBs, which hold great application potential in large-scale energy storage. Cathode materials with excellent electrochemical performance are in urgent demand for next-generation SIBs. Herein, this review provides a comprehensive overview of the recent advances of the most promising SIBs cathode candidates, including layered oxides, polyanionic materials, and Prussian blue analogues. The currently existing issues that need to be addressed for these cathodes are pointed out, such as insufficient energy density, low electron conductivity, air sensitivity, and so on. This review also details the structural characteristics of these three cathode candidates. Moreover, the recent optimization strategies for improving the electrochemical performance are summarized, including element doping, morphology modification, structure architecture, and so on. Finally, the current research status and proposed future developmental directions of these three cathode materials are concluded. This review aims to provide practical guidance for the development of cathode materials for next-generation SIBs.

1. Introduction

Due to the overuse and adverse environmental impact of traditional fossil fuels, the development of renewable and green energy resources has become more significant than ever. In recent years, considerable research has been dedicated to exploring new energy sources, including hydrogen energy, wind energy, solar energy, hydro energy, tidal energy, and so on.^[1–4] However, these new energy sources are intermittent, necessitating the use of energy storage devices. Electrochemical storage devices play an indispensable role due to their overwhelming advantages such as season/weather independence, high energy efficiency, continuity, and portability. Notable examples of these devices include lithium-ion batteries (LIBs), potassium-ion batteries, and zinc-air batteries, etc. Furthermore, The Nobel Prize in Chemistry 2019^[5] was awarded to John B. Goodenough,^[6,7] M. Stanley Whittingham,^[8,9] and Akira Yoshino,^[10] in recognition of their contributions to the development of LIBs. This prestigious award confirms the importance of LIBs as

one of the key electrochemical energy storage systems in addressing global energy challenges and has triggered a new wave of research in this field.

C. Peng, F. Li, L. Xi, J. Zeng, X. Song, X. Wan, J. Liu
School of Materials Science and Engineering
Guangdong Provincial Key Laboratory of Advanced Energy Storage Materials
South China University of Technology
Guangzhou 510641, China
E-mail: msjliu@scut.edu.cn

 The ORCID identification number(s) for the author(s) of this article can be found under <https://doi.org/10.1002/sstr.202300150>.

© 2023 The Authors. Small Structures published by Wiley-VCH GmbH. This is an open access article under the terms of the Creative Commons Attribution License, which permits use, distribution and reproduction in any medium, provided the original work is properly cited.

DOI: 10.1002/sstr.202300150

X. Xu
College of Chemical Engineering and Light Industry
Guangdong University of Technology
Guangzhou 510006, China
E-mail: xuxijun2022@gdut.edu.cn

J. Zhao
Research and Development Center
Guangzhou Tinci Materials Technology Co., Ltd.
Guangzhou 510765, China
E-mail: zhaojingwei@tinci.com

Up to now, LIBs have been commercially applied in electric vehicles, portable electrons, and large-scale energy storage systems, owing to their long cycle life, high output voltage, and energy density.^[11–14] However, the widespread application of LIBs is severely hampered by the limited lithium salt and high cost. Additionally, advancements in LIBs seem to have nearly reached a plateau in terms of cycle life, capacity, and energy density.^[15] Recent researches show that the energy density of commercial LIBs has achieved 250–450 Wh kg⁻¹, together with high rate performance (within 12 mins charging a 265 Wh kg⁻¹ battery from 0% to 75%) and nearly 100% efficiency.^[16] Nevertheless, the limited lithium resources constrained the wide commercial application of LIBs and thus necessitating the search for alternatives. According to statistics, the prices of Li edged up 300% in 2022 compared to 2021.^[17] Furthermore, the uneven distribution and mining of Li resources also escalated the cost related to transportation, labor, and the environment.^[16] As this trend continues, LIBs gradually become insufficient to support the thriving development of electric vehicles and large-scale energy storage. Therefore, the exploration of alternatives, such as next-generation rechargeable batteries, cannot be delayed.

Fortunately, sodium resources are abundant and distributed widely on the earth's crust, with a content of 2.3% compared to that of lithium only 20 ppm.^[18] Furthermore, sodium salt has the advantage of low cost, and the processes of mining metal Na are also simpler and more environmentally friendly. Actually, Na ions were discovered to possess high conductivity at ambient temperatures first in 1967, opening a new perspective for the large-scale energy storage system. Since then, research on sodium-ion batteries (SIBs) has never stopped.^[19] However, due to the inferior energy density and cycle life of SIBs compared to LIBs, most researchers paid more attention to LIBs, thereby slowing down the development of SIBs. It was not until the 2000s, when SIBs were discovered to have a high reversible capacity of 300 mAh g⁻¹,^[18] that they began to attract unprecedented attention once again. Generally, SIBs have the highlighted advantages of safety, low cost, and wide comfort temperature zone. Additionally, both LIBs and SIBs belong to the "rocking-chair"^[20] battery, indicating SIBs are promising alternatives to LIBs in the field of large-scale energy storage. However, despite the similarities in charge-discharge mechanisms, components, and fabrication equipment between LIBs and SIBs, it is not feasible for SIBs to unreservedly mimic LIBs. As shown in Table 1, the ionic radius of Na (1.02 Å) is larger than that of

Li (0.76 Å), which is a critical factor that differentiates LIBs from SIBs. Most electrode materials in SIBs/LIBs are Na/Li compounds with crystallographic-layered structures, and Na⁺/Li⁺ inserting/extrating between interlayers during charging/discharging processes. Due to the larger ionic radius of Na⁺ case volume change for SIBs is larger than that of LIBs, resulting in various phase transformations during Na⁺ insertion.^[21] Apart from ionic radius, different densities, atomic weight, ionization energy, and redox potential limit the direct imitation as well.^[22] For instance, lower ionization energy means lower activation energy for Na⁺ diffusion compared to Li⁺.^[18] Generally, SIBs are preferable to be applied in large-scale energy storage, which does not demand as high as electric vehicles do.^[23]

Overall, thanks to low cost and pollution, SIBs are promising alternatives for LIBs. However, their energy density remains insufficient and urgently needs improvement. A big challenge is the selection of cathode material. So far, a wide range of families of cathode materials have been synthesized and published in research articles focusing on optimizing the electrochemical performance of SIBs: layered oxides, polyanionic compounds, Prussian Blue analogs (PBAs), and organics, where the first three types draw the most attention. Thereinto, layered oxides are recognized for their distinct layered structures and relatively high energy densities, which significantly contribute to their broad application in energy storage systems. Polyanionic compounds are appreciated for their robust crystal structures that provide notable stability during cycling, achieving superior cycle life. Additionally, they exhibit high thermal stability beneficial for safety considerations. Prussian Blue analogs, on the other hand, have a three-dimensional crystal structure with large interstitial spaces. This characteristic enables fast ion diffusion, thereby facilitating high-rate capability, making PBAs particularly suitable for applications requiring rapid charge and discharge cycles. In this review, an overview of layered oxides, polyanionic compounds, and Prussian Blue analogs regarding the classification of structures and challenges are described. After that, optimization strategies of these three kinds of material as cathode materials published in recent years are summarized, emphasizing the element doping, surface coating, structure architecture, and synthetic methods, as shown in Figure 1. Finally, the three materials are compared from the perspectives of electrochemical performance, cost, and environmental friendliness.

2. Structure Features and Current Issues of Promising Cathode Candidates

The cathode materials for SIBs cover a wide range of families with diverse structures allowing Na⁺ insertion/extraction. A desired cathode material for SIBs is supposed to possess various characteristics, such as high energy density, high output voltage, long life cycle, excellent rate performance, high chemical and structural stability, high safety, low cost, and so on. Layered oxides, polyanionic compounds, and Prussian Blue analogs are the most promising candidate materials, which are introduced in the following briefly in terms of structure evolution and current challenges.

Table 1. Comparison of parameters between sodium and lithium.

	Na	Li	References
Material abundance [ppm]	23 600	20	[18]
Ionic radius [Å]	1.02	0.76	[16]
Density [g cm ⁻³]	0.971	0.534	[22]
Atomic weight [mol g ⁻¹]	23.0	6.9	[50]
Theoretical capacity of metal electrodes [mAh g ⁻¹]	1166	2861	[18]
Ionization energy [eV]	5.14	5.39	[16]
E° versus SHE [V]	-2.71	-3.04	[34]

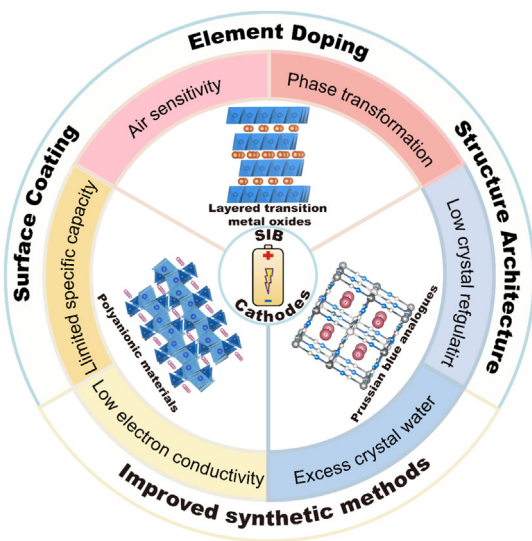


Figure 1. Schematic illustration of candidate cathodes for SIBs: layered transition metal oxides, polyanionic materials, and Prussian blue analogous.

2.1. Layered Oxides

2.1.1. Classification and Structure Features of Layered Oxides

With a general formula of Na_xMO_2 , where M represents 3d transition metal elements, layered oxides have a dominant superiority beyond LIBs: from Ti to Ni, all 3d transition metals can be utilized as components, whereas in Li_xMO_2 , only Ni and Co can be applied to form a stable layered structure.^[24] By the way, except for the layered structure, Na_xMO_2 can also adopt a tunnel structure. While the tunnel structure is convenient for Na^+

diffusion, it limits the reversible insertion/extraction of Na^+ between interlayers, causing limited capacity.^[25]

Generally, the layered structure of Na_xMO_2 is built up by the cross-arranged transition metal sheets and alkalis sheets along the c-axis direction (Figure 2a–b). The transition metal sheets are formed by interconnected MO_6 octahedral units through sharing edges, while Na^+ ions locate between the transition metal sheets, forming an alkalis sheet. Based on the different Na^+ polyhedral coordination geometries and the stacking patterns of O^{2-} , Delmas et al.^[26] classified these structures into four categories: P2 type, P3 type, O2 type, and O3 type. The letters “O” and “P” denote the Na^+ ions located in an octahedral environment and trigonal prismatic environment, respectively. The numbers “2” and “3” suggest the number of minimum layers of oxygen packing. If there is a prime or a double prime on the symbol, it suggests that monoclinic/orthorhombic distortion or triclinic distortion of the hexagonal lattice.^[21]

The P2- and O3-layered oxides are the currently most researched types. With a space group of $P6_3/mmc$, P2- Na_xMO_2 exhibits AB BA oxygen packing arrangement of MeO_2 slabs (Figure 2a). This structure is formed by the stacking of MO_6 and NaO_6 , along the direction perpendicular to [111]. The P2-type-layered oxide possesses superior rate performance and structure stability because Na content in this structure is relatively low (typically $x < 0.68$ in Na_xMO_2) compared to O-type structures, which allows for facile Na^+ diffusion due to the presence of vacancies. Besides, a P2-O2 phase transition may occur during the charging process at high voltage or high temperature, leading to the breakage of the M–O bond.

In the case of O3- Na_xMO_2 , Na content is higher compared to the P2 type and x is almost equal to 1. The O3 phases belong to one of the cation-ordered rock-salt superstructure oxides and are classified as 3R phases with a space group of $R\bar{3}m$.^[18] However, during discharge processes, the structure tends to be unstable.

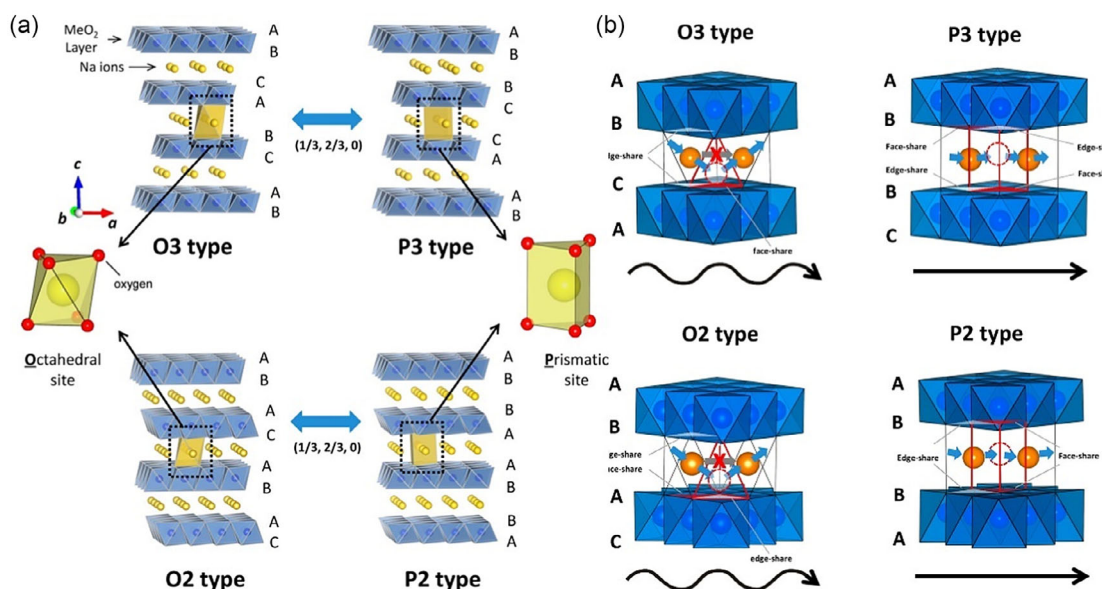


Figure 2. a) Crystal structure and b) Na ions diffusion path of different layered transition metal oxides. Reproduced with permission.^[18] Copyright 2014, American Chemical Society.

This is because MO_2 slabs undergo gliding after partial Na^+ extraction, resulting in the original oxygen packing order changing from AB CA BC to AB BC CA. As a consequence, Na^+ ions shift from octahedral sites to prismatic sites, leading to an O3-P3 phase transformation. Unlike the P2 phase, in the O3 phase, the MO_2 slabs be able to glide without breakage of M–O bonds, which means it is much easier to occur and causes the structure of O3 to be less stable than the P2 phase.

In terms of rate performance, Na^+ ions in P2 structures can migrate directly from one prismatic site to another adjacent site, as depicted in Figure 2a. On the other hand, Na^+ ions in O3 structures must first migrate from an octahedral site to a tetrahedral site and then to the adjacent octahedral site, due to the higher diffusion barrier.^[18] This difference in migration pathways explains why the rate performance of the O3 phase is inferior to that of the P2 phase. It is worth noting that commonly observed layered oxides NaMO_2 with M=Ti, V, Cr, and Fe exhibit the O3 phase, while NaMO_2 with M=Mn, Ni, and Co exhibit the P2 phase.^[21]

2.1.2. Current Issues of Layered Oxide

As for layered oxides, three primary current issues are well acknowledged, which are irreversible phase transition, lack of energy density, and high air sensitivity, respectively.

To differentiate the variable phases of layered oxides, Zhao et al. introduced the concept of “cationic potential” as an indicator, which is based on the parameters of the weighted average ionic potential of TMs, the weighted average ionic potential of Na, and the ionic potential anion of oxygen ions. The P2 phase is characterized by a high cationic potential, which is attributed to the high interlayer electrostatic repulsion. On the other hand, the O3 phase is characterized by a high ionic potential due to its high Na content.^[27] However, the phases of layered oxides may undergo changes during Na^+ insertion/extraction processes due to the occurrence of undesirable irreversible phase transitions. Typically, both P2 and O3 phases suffer from variable phase transitions due to stacking faults or intergrowth of the oxide layers.^[28] As for the P2 phases (Figure 2a), the P2 phase transforms into the O2 phase under high-temperature conditions. After Na^+ extraction, Na^+ ions turn to locate at octahedral TMO_2 sites instead of prismatic TMO_2 sites. Additionally, the order of oxygen packings also changes from “AB BA AB” to “AB AC AB”. In the case of O3 phases, there are more complicated transitions because octahedral sites are less stable than prismatic sites in the P2 phase. Take $\text{NaNi}_{0.5}\text{Mn}_{0.5}\text{O}_2$ ^[29] as an example, crystal structure undergoes phase transitions of $\text{O}_3 \rightarrow \text{O}'_3 \rightarrow \text{P}_3 \rightarrow \text{P}'_3 \rightarrow \text{P}''_3$ during Na^+ extraction. Notably, all O3 phase Na_xTMO_2 will undergo O3-P3 transition after approximately 25% Na^+ ions are extracted.^[30] Multiple complicate phase transitions would lead to structure instability or even destruction, which is a crucial issue needed to be tackled urgently.

In addition to complex phase transitions, instability of storage in the air is another challenge that constrains the development of layered oxides. When Na^+ ions are extracted in the air, undesired chemical reactions are easy to occur between the layered oxides and substances including H_2O , CO_2 , and O_2 . Notably, in the internal bulk phase, H_2O and CO_2 molecules will be embedded

in the TMO_2 slabs, rather than just be absorbed on the surface.^[31] Moreover, O_2 will oxidize the TMs, such as Fe^{2+} and Mn^{3+} in layered oxides.^[32] This oxidation reaction would impair the original structure and electrochemical performance of the materials. When exposed to air, the layered transition metal oxides undergo an oxidation reaction with water molecules, which leads to the H^+/Na^+ exchange and production of NaOH .^[32] Worse still, water-soluble CO_2 also participates in H^+/Na^+ exchange and generates Na_2CO_3 . This process facilitates the decreased content of Na^+ ions and causes larger crystal lattice space, due to increased repulsion between adjacent oxide layers and an unstable framework. Besides, the formation of carbonate would deteriorate the surface and increase the acidity of materials as well. These air-induced reactions pose significant challenges to the stability and performance of layered oxides in practical applications.

Electrochemical performance plays a crucial role application of SIBs for energy storage systems, which rely on specific capacity, output voltage, and cycling life. However, the presence of complex irreversible phase transitions and air sensitivity often hampers the achievement of satisfactory energy density in these materials. On one side, irreversible phase transition and air sensitivity cause rapid capacity decay, on the other side, the high cut-off voltage will facilitate undesired complex phase transition. Additionally, though many redox couples, such as $\text{Fe}^{3+}/\text{Fe}^{4+}$, $\text{Co}^{3+}/\text{Co}^{4+}$, $\text{Cr}^{3+}/\text{Cr}^{4+}$, $\text{Mn}^{3+}/\text{Mn}^{4+}$, and $\text{Ni}^{2+}/\text{Ni}^{4+}$,^[29] deliver relatively high redox potential and enable to provide relatively high reversible capacity, there are still some issues to be addressed, such as Jahn-Teller effects of Mn^{3+} , the toxicity of Cr, and the high cost of Co.^[33] On account of this, to maintain the relatively high capacity as well as high redox potential, optimization strategies play an indispensable role.

Therefore, efforts to improve the electrochemical performance of layered oxides are essential, taking into consideration factors such as air stability, specific capacity, and phase transition. Addressing these limitations is crucial to meet the requirements of practical applications.

2.2. Polyanionic Compounds

2.2.1. Classification and Structure Features of Polyanionic Compounds

With the formula of $\text{Na}_x\text{M}_y(\text{XO}_4)_n$, ($\text{X}=\text{S}, \text{P}, \text{Si}, \text{As}, \text{Mo}$, and W , $\text{M}=\text{transition metal}$),^[34] polyanionic cathode materials have the characteristics of high redox potential and high thermal stability while low electrical conductivity. Due to the variety of M and X, many kinds of polyanionic materials have been applied in SIBs. In this section, we will primarily introduce phosphates, pyrophosphates, fluorophosphate, sulfates, and silicates as examples of polyanionic cathode materials.

Derived from LiFePO_4 cathode material in LIBs, phosphates NaMPO_4 ($\text{M}=\text{Fe, Mn}$) show outstanding commercialization as well. Among them, NaFePO_4 exhibits remarkable commercial potential. NaFePO_4 with an orthorhombic crystal structure (space group: Pnma)^[35] has two phases which are olivine and maricite, respectively.^[36,37] Due to the existence of Na^+ ions diffusion channel along the b -axis in olivine structure, formed by the connection of corner shared FeO_6 units and PO_4 tetrahedron

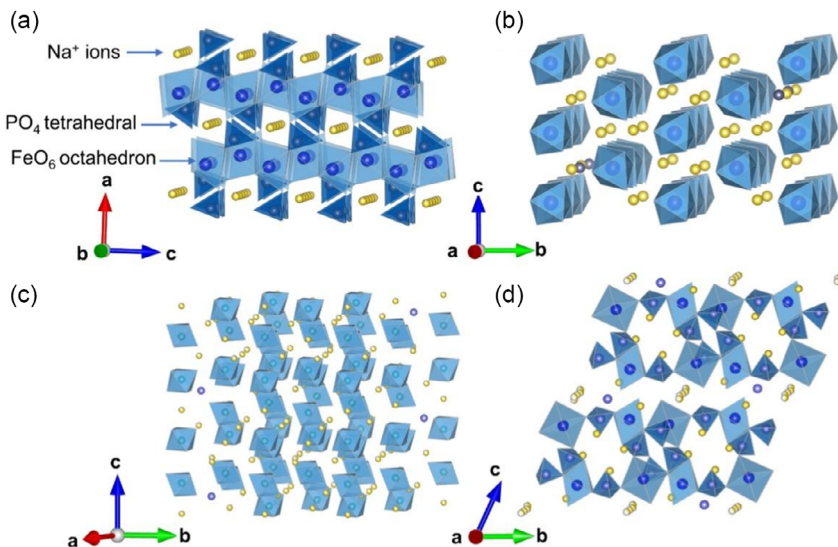


Figure 3. Schematic illustration of the crystal structure of a) NaFePO_4 (olivine-type), b) NaFePO_4 (maricite-type), c) $\text{Na}_3\text{V}_2(\text{PO}_4)_3$, and d) $\text{Na}_2\text{FeP}_2\text{O}_7$.

(Figure 3a,b), the olivine NaFePO_4 is extremely promising as SIBs cathode material for its high capacity. In contrast, the maricite phase lacks Na^+ ions diffusion channel, which is undesired. Consequently, the phase transition from olivine to maricite at high temperatures is considered undesirable. To address this issue, olivine NaFePO_4 is usually synthesized by ion-exchanging from LiFePO_4 instead of traditional chemical reactions.^[38] As for NaMnPO_4 , it has the superiority of high capacity. However, the risk of dissolution of Mn into the electrolyte and the corresponding Jahn–Teller effect constrain its development, which needed to be optimized urgently.^[39]

Compared to the single diffusion channel of NaMPO_4 , NASICON-type (Na Super Ionic Conductor) phosphate materials have multiple 3D Na^+ transport channels which allow faster Na^+ diffusion. The basic formula of NASICON-type phosphate materials is $\text{Na}_x\text{M}_2(\text{XO}_4)_3$ ($\text{M}=\text{V, Fe, Ni, Mn, Ti Cr, Zr, etc.}$, and $\text{X=P, S, Si, Se, Mo}$). In the aspect of transition metal, NASICON-type phosphate materials can be categorized into single transition metal types and binary transition metal types. Among single transition metal types, $\text{Na}_3\text{V}_2(\text{PO}_4)_3$ (NVP) is particularly investigated, showing prominent advantages of thermal stability, long life cycle, and low volume expansion.^[40] The structure of NVP features a space group of $\text{R}\bar{3}\bar{c}$. It consists of VO_6 octahedra connected to three PO_4 tetrahedra through oxygen atoms, forming a “lantern” unit (Figure 3c). Within this 3D framework, there are $\text{Na}1$ sites (sixfold coordination) and $\text{Na}2$ sites (eightfold coordination). The $\text{Na}1$ sites exhibit higher electrochemical activity, and Na^+ ions are extracted from the interlayers at higher voltages compared to the $\text{Na}2$ sites. Besides, the open 3D framework provides multiple migration routes for Na^+ ions diffusion. However, the isolated metal octahedrons cause low electronic conductivity. About binary transition metal type $\text{Na}_x\text{M}_1\text{M}_2(\text{PO}_4)_3$, their predominant advantage is decreasing cost and environmental pollution by substituting partial vanadium in NVP.^[34] Moreover, some other transition metal elements such as Ti and Mn can also help to improve the capacity and reduce side reactions.^[41]

Pyrophosphates are derived from phosphates through thermal decomposition at 500–550 °C.^[34] During this process, an oxygen atom is lost, leading to the formation of a P_2O_7 unit. Consequently, pyrophosphates exhibit better structure stability compared to phosphates though may sacrifice some specific capacities. There are totally 3 kinds of pyrophosphates: NaMP_2O_7 , sodium bimetallic pyrophosphates $\text{Na}_2\text{MP}_2\text{O}_7$, and the mixed metal sodium pyrophosphates $\text{Na}_4\text{M}_3(\text{PO}_4)_2\text{P}_2\text{O}_7$, respectively.^[42] $\text{Na}_2\text{MP}_2\text{O}_7$ is of special concern,^[43] similar to NVP, which is composed of the corner-connected FeO_6 octahedron and PO_4 tetrahedron, and there are also 3D Na^+ ions diffusion channel constructed by P_2O_7 polyhedral in directions of [100], [110], and [011] (Figure 3d).^[43] $\text{Na}_2\text{MP}_2\text{O}_7$ has a relatively high operating voltage, while low capacity, approximately 90 mAh g⁻¹. The low capacity is arisen from the multiple extraction steps of Na^+ ions in different circumstances (Na1–Na8) and ordering.^[44]

Fluorophosphate materials are formed by incorporating fluorine ions into phosphate compounds. Fluorophosphate can be classified into three kinds, which are NaVPO_4F , $\text{Na}_2\text{MPO}_4\text{F}$, and $\text{Na}_3(\text{VO}_{1-x}\text{PO}_4)_2\text{F}_{1+2x}$ ($0 \leq x \leq 1$), respectively.^[42] Particularly, the sodium vanadium fluorophosphate family attracts the most attention. For instance, the sodium vanadium fluorophosphate NASICON-type $\text{Na}_3\text{V}_2(\text{PO}_4)_2\text{F}_3$ can reach a high operating voltage of 3.66–4.1 V.^[45] $\text{Na}_2\text{FePO}_4\text{F}$ ^[43] and $\text{Na}_2\text{CoPO}_4\text{F}$ ^[46] are also promising SIB candidate cathodes waiting to be researched.

Sulfates ($\text{Na}_2\text{M}(\text{SO}_4)_2\cdot n\text{H}_2\text{O}$) attract worldwide interest for the more ionic M–O bond and stronger electronegativity of SO_4^{2-} than that of phosphate.^[34] Among the various sulfates, $\text{Na}_2\text{Fe}_2(\text{SO}_4)_3$ is the most promising one. In the structure of $\text{Na}_2\text{Fe}_2(\text{SO}_4)_3$, there exists a 3D Na^+ diffusion channel which is composed of dimer Fe_2O_{10} polyhedral and SO_4 units.^[47] Silicates (Na_2MSiO_4) are also worth mentioning, which are famous for their high structure stability owing to the strong Si–O bond.^[34] A representative example is $\text{Na}_2\text{FeSiO}_4$, which

shows a theoretical capacity of 276 mAh g⁻¹ and undergoes two electrons transfer during charge/discharge processes.^[48]

2.2.2. Current Issues of Polyanionic Materials

Polyanion-type material cathodes have relatively high redox potential, which is attributed to the inductive effect induced by the presence of high electronegative polyanion groups.^[49] However, the large particle size, elevated molar mass, and inferior intrinsic electron conductivity of polyanionic groups ultimately diminish the net electrochemical specific capacity and further hinder the development.

Polyanionic compounds suffer from possessing the drawback of intrinsic low electron conductivity because of the absence of direct electron delocalization.^[50] Though NASICON-type phosphate has multiple fast Na⁺ transportable 3D channels, the electron conductivity is still unsatisfactory. For example, in NASICON-type Na₃V₂(PO₄)₃, there is no O atom shared between the VO₆ octahedra while shared in the PO₄ tetrahedron, resulting in the electrons transfer following a V–O–P–O–V route, instead of a speedy V–O–V path.^[34] Therefore, despite high output voltage and stable structure, polyanionic compound cathode materials still face challenges to fully achieve commercialization, and low conductivity is one of the most urgent problems to be solved. Low electron conduction would further influence rate capability and then diminish the specific capacity. As we all know, a high specific capacity is typically achieved through the insertion and extraction of multiple ions. However, in polyanionic materials, not all Na⁺ ions can escape from the framework, only about 50% according to the ref. [37]. Additionally, large molecular weight also suppresses the specific capacity, indicating that polyanionic material is still away from being theoretical cathode materials.^[51]

2.3. Prussian Blue Analogues

2.3.1. Classification and Structure Features of Prussian Blue Analogues

Prussian blue (PB) and its analogues (PBA) are favorable as SIB cathode candidates for their high redox potential, facile synthesis methods, and high structure stability. PB, also known as ferric ferrocyanide, has the chemical formula of A_xFe[Fe(CN)₆]₃·nH₂O, where A represents an alkali metal element. PBA, on the other hand, has a more complex formula of (A_xM₁[M₂(CN)₆]_{1-y}·□_y·nH₂O (metal hexacyanometallates), where A refers to alkali metal element, M₁ and M₂ refer to the transition metals connected with CN ligands, and □ refer to the vacancies in PBA. Many oxidation sites are located in their structures and energy density can reach 500–600 Wh Kg⁻¹.^[52] As shown in Figure 4a,b,^[53] both PB and PBA show a perovskite structure with a space group of Fm3m. In PB, there are two distinct Fe oxidation states: low-spin Fe^{LS}(C) located adjacent to the C atom and high-spin Fe^{HS}(N) coordinated with the N atom. And Fe^{HS}(N) is more chemical active than Fe^{LS}(C). Due to the mixed-valence and quantity variance between Fe²⁺ and Fe³⁺, many vacancies filled with H₂O molecules existed in the framework, to maintain neutrality of the whole structure. By the way, both coordination water and interstitial water are harmful to the electrochemical performance.^[53] As for the bonding strength of Fe²⁺ and Fe³⁺, the interaction between the C atom and Fe²⁺ is stronger. This is because the Fe²⁺ ion shows a strong covalent interaction due to a d⁶ electronic configuration, whereas the Fe³⁺ ion is in a d⁵ electronic configuration, indicating weaker ionic bonding with N atoms. Thus, in [Fe(CN)₆]⁴⁻ unit the Fe²⁺ is hard to be replaced by other transition metals.^[54] Furthermore, the phases of PB and PBAs can vary depending on the content of

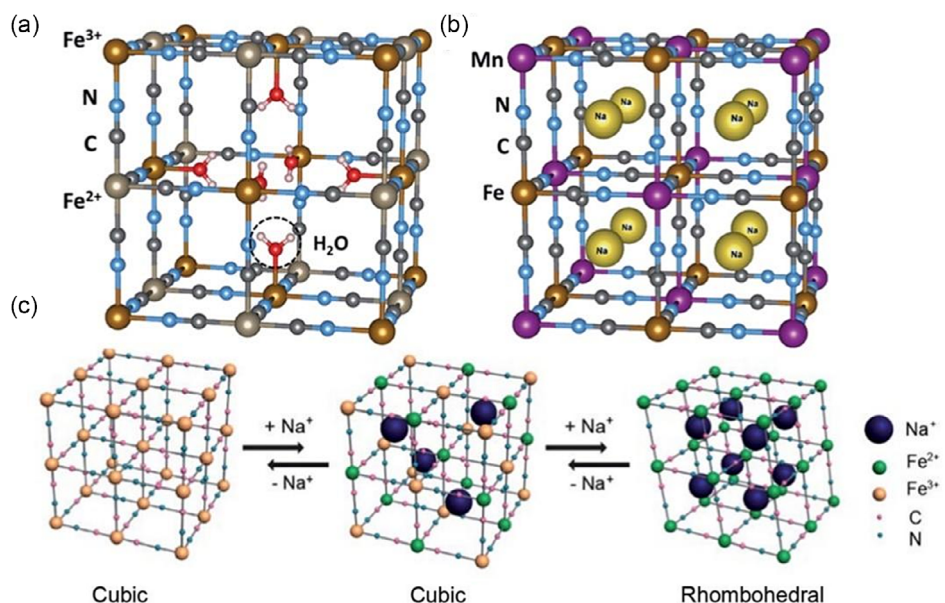
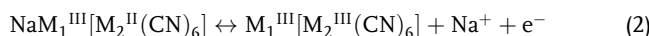
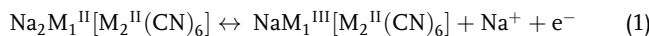


Figure 4. Crystal structure of a) Prussian blue (PB) $\text{Fe}_4[\text{Fe}(\text{CN})_6]_3 \cdot n\text{H}_2\text{O}$ and b) Prussian blue analog (PBA) $\text{Na}_x\text{MnFe}(\text{CN})_6$. Reproduced with permission.^[53] Copyright 2017, Royal Society of Chemistry. c) Phase transformation of PB during charge/discharge processes. Reproduced with permission.^[56] Copyright 2014, Royal Society of Chemistry.

interstitial water, vacancies, and Na^+ ions, with possible classifications including monoclinic, rhombohedral, cubic, and tetragonal structures.^[54] During the charging process, with increasing alkaline content, the phase of PB would change from cubic to rhombohedral (Figure 4c).^[55,56]

PBAs, which are cyanide derivatives of PB, can be synthesized by substituting Fe ions with other transition metal elements such as Mn, Co, Ni, Cu, and Zn.^[53] As presented in Figure 4b, there are open Na^+ ions diffusion channels and interstitial positions contained in the 3D structure as well. Partial interstitial 8c positions are filled with Na ions. The interstitial positions in PBAs have a diameter of approximately 4.6 Å, while the spacious channels have a diameter of 3.2 Å in the <100> direction,^[57] implying a reversible fast electron transportation. It is noteworthy that PBAs can be classified into two kinds: SE-PBAs and DE-PBAs, according to the number of redox couples. The former contains only one redox couple whereas the latter possesses two, enabling a two- Na^+ ions-transportation during reversible/discharge processes in each unit. The redox mechanisms of SE-PBAs follow only the first equation while of DE-PBAs follow the equations.^[58]



Additionally, in the aspect of structure evolution, the phase transitions during Na^+ ions diffusion are more complicate compared to PB. For example, Mn-PBAs exhibit phase transitions of monoclinic \leftrightarrow cubic \leftrightarrow tetragonal,^[58] Co-PBAs undergo transitions of Monoclinic \leftrightarrow Cubic \leftrightarrow Tetragonal,^[59] Fe-PBAs show phase transitions of Rhombohedral \leftrightarrow Cubic \leftrightarrow Tetragonal.^[60] Nevertheless, so far, the structure evolution of PBAs has not been comprehensively revealed, which still needs further study.

2.3.2. Current Issues of Prussian Blue Analogues

Despite the advantages of PBAs such as high redox potential, high thermal stability, and large Na^+ ion diffusion channels, PBAs as cathode material for SIBs still cannot exhibit a satisfactory electrochemical performance owing to the shortcomings of excess crystal water, imperfect crystal structure, and low capacity, which are demonstrated later.

To date, there is not as much published research on PBAs as layered oxides and polyanionic materials, thus, synthetic methods for the preparation of PBAs are not perfect enough. Typically, most PBAs are fabricated from liquid solution, which can introduce crystal water, including coordinated water and interstitial water, as well as vacancies in the $\text{Fe}(\text{CN})_6$ framework.^[61] As shown in Figure 4a,b, the presence of interstitial water molecules, with an oxygen atom forming a bond with a transition metal element, can have a detrimental effect on PBAs. Besides, according to some research, there is approximately 15% of interstitial water contained in PBA.^[62] Indeed, the interstitial water molecules tend to compete with Na^+ ions for the host sites, then impede the transportation of Na^+ within the framework, and further influence the Na^+ insertion/extraction process. This interference hampers the rate performance and specific capacity of PBAs as cathode materials for SIBs. In addition, the residual interstitial water not only

competes with Na^+ ions for host sites but also possibly dissolves in and reacts with the electrolyte. This can lead to the collapse of the framework structure and deteriorate the cycling performance of the PBAs. Worse still, if the electrolyte is specific organics, adverse by-products^[33] and safety accidents might also be brought about.^[57] Moreover, the random distribution of vacancies in the PBA structure can impede the electron transport along the M1-CN-M2 pathway, resulting in increased Ohmic polarization and reduced overall electrochemical performance.^[54,57]

Because of the two-electron redox reaction, PBAs theoretically have a relatively high capacity,^[56] for example, 209 mAh g⁻¹ for $\text{Na}_2\text{Mn}[\text{Mn}(\text{CN})_6]$.^[63] However, the excess interstitial water and vacancies in $\text{Fe}(\text{CN})_6$ in the framework would hinge migration of Na^+ ions, leading to low crystal regularity, decreased capacity, lower Coulombic efficiency, and structure destruction. Furthermore, structure evolution is another factor determining the capacity of PBAs. Overall, to cope with these drawbacks, suppressing the content of excess water and vacancies in $\text{Fe}(\text{CN})_6$ is the main task to achieve a satisfying electrochemical performance for PBAs cathode material.

3. Optimization Strategies for Layered Transition Metal Oxide

Layered oxides have emerged as promising candidate cathode materials for their remarkable properties of high capacity, facile synthesis methods, and so forth. However, they are also confronted with significant challenges that require attention. To enhance their electrochemical performance, extensive research has been conducted to optimize their structure stability and output voltages. The optimization strategies could be concluded in three aspects: element doping, surface coating, and structure architecture.

3.1. Element Doping

Layered oxides incorporate a range of transition metals as their components, each offering distinct characteristics. For instance, nickel (Ni) exhibits a high voltage range, while iron (Fe) and manganese (Mn) are known for their high capacity. These variations in elemental composition contribute to the diverse electrochemical properties and performance of layered oxides. Initially, layered oxides Na_xCoO_2 ,^[64–66] Na_xCrO_2 ,^[67–70] Na_xMnO_2 ,^[71–74] and $\alpha\text{-NaFeO}_2$,^[75–77] etc., were identified suitable as host materials for Na^+ ions insertion/extraction in SIBs.^[78] However, Na_xMO_2 with a single transition metal element was later recognized that were unable to fulfill the comprehensive requirements necessary for efficient energy storage. It is of great significance to design layered oxides containing multiple transition metals as it allows for the utilization of their synergistic advantages. Take O3-type $\text{Na}_4\text{FeRuO}_6$ ^[71] as an example, it demonstrates the benefits of incorporating ruthenium (Ru) alongside iron (Fe). The partial substitution of Fe with Ru in $\text{Na}_4\text{FeRuO}_6$ can help to reduce particle cracking, thereby improving the electrochemical performance of the material. Based on this point, the introduction of element doping in layered oxides, incorporating binary, ternary, or even multiple transition metal elements, has emerged as a viable strategy. Element doping is considered a valid strategy

to increase the average working voltages, activate anionic redox reaction, and enhance structure stability, which is implemented by substituting partial elements with single or multiple other ions. Generally, the commonly employed elements for layered oxides are Ni, Ca, Zn, Al, Ti, Co, etc.^[79–83] Each element possesses its unique properties, enabling the enhancement of the electrochemical performance of layered oxides through tailored doping strategies.

3.1.1. Increase the Average Working Voltage

As earlier mentioned, complex phase transition leads to capacity decay and structural instability. Irreversibly complex phase transition and other adverse side reactions between cathodes and electrolytes occur especially under high operating voltage, which seriously hampered the commercial application of layered oxides.^[79] In this case, doping of specific transition metal elements can effectively tackle the issues under high output voltages and further improve energy density.

Mn-based Na_xMO_2 materials have a common failing that at high voltage Mn dissolution will induce the Jahn-Teller effect. Zhao et al.^[79] prepared a Ti-doped P2- $\text{Na}_{0.66}\text{Mn}_{0.54}\text{Ni}_{0.13}\text{Co}_{0.13}\text{O}_2$ (Ti-MNC) cathode material. By introducing Ti doping, a new titanium gradient design was proposed, where the Ti-rich surface and Ti-substituted interior work synergistically. Owing to the similar properties of Mn^{4+} and Ti^{4+} such as ionic radius and valence state, Ti^{4+} ions can be doped into the transition metal layers easily

without destroying the structure, which increased the lattice spacing of the structure and further facilitate the electron transfer kinetics. Besides, the Ti-doped surface plays a role in restraining side-reactions between electrolyte and electrode and relieving Jahn-Teller distortion under high working voltage. Thereby a remarkable electrochemical performance is achieved with a high cut-off voltage of 4.7 V at 1 C and a high energy density of 456.4 Wh kg⁻¹. Similarly, Yang et al.^[80] synthesized Cu-doped $\text{Na}_{0.67}\text{Ni}_{0.33-x}\text{Cu}_x\text{Mn}_{0.67}\text{O}_2$ cathode for SIBs. By substituting Cu for a portion of Mn, more Na^+ sites were retained, alleviating the P2-O2 phase transition at high voltage. Furthermore, the Cu substitution helped suppress Jahn-Teller distortion caused by Mn. Moreover, it is discovered that the $\text{Cu}^{2+}/\text{Cu}^{3+}$ redox couple also contributes to the reversible capacity, finally, this material shows a reversible capacity of 62 mAh g⁻¹ at 20 C and a wide voltage range from 2 to 4.3 V (Table 2). Zhang's group^[84] presented an Mg-doped P2- $\text{Na}_{0.67}\text{Ni}_{0.33}\text{MnO}_2$ (NNMMO) cathode material restraining Jahn-Teller distortion successfully, in which a novel ZrO_2 coating surface modification is applied to mitigate side reactions between cathode and electrolyte. Mg dopant induces the reversible P2-OP4 phase transition and inhibits destructive P2-O2 phase transition occurring at higher voltages. Finally, NNMMO cathode material exhibits a high working voltage of 3.57 V with an energy density of 238.91 Wh kg⁻¹ (Table 2). However, the cation doping described above can efficiently improve cutoff voltage to some extent, it may sacrifice capacity by inactive TM cation substitution. It is important to strike a balance between achieving a high

Table 2. Electrochemical performance comparison of reported layered oxides.

Cathode materials	Optimization strategy	Phase	Voltage [V]	Reversible capacity [mA h g ⁻¹]	Capacity retention	References
Ti-doped $\text{Na}_{0.66}\text{Mn}_{0.54}\text{Ni}_{0.13}\text{Co}_{0.13}\text{O}_2$	Element doping	P2	4.70	133.2 at 0.1 C	77.9% after 100 cycles	[79]
Cu-doped $\text{Na}_{0.67}\text{Ni}_{0.33-x}\text{Cu}_x\text{Mn}_{0.67}\text{O}_2$	Element doping	P2	4.30	120.0 at 1 C	78% after 200 cycles	[80]
Mg-doped $\text{Na}_{0.67}\text{Ni}_{0.33}\text{MnO}_2$	Element doping	P2	3.57	143.3 at 0.1 C	84.7% after 50 cycles	[84]
F, Mg-doped $\text{Na}_{0.67}\text{Ni}_{0.15}\text{Fe}_{0.2}\text{Mn}_{0.65}\text{F}_{0.05}\text{O}_{1.95}$	Element doping	P2	4.20	229.0 at 0.1 C	87.7% after 50 cycles	[86]
Sb-doped $\text{Na}_{0.67}\text{Mn}_{0.66}\text{Ni}_{0.33}\text{O}_2$	Element doping	P2	4.20	130.0 at 1 C	86% after 200 cycles	[87]
Co-doped Na_2RuO_3	Element doping	O3	4.30	177.0 at 0.2 C	74% after 300 cycles	[96]
$\text{Na}_{0.85}\text{Ni}_{0.34}\text{Mn}_{0.33}\text{Ti}_{0.33}\text{O}_2$	Element doping	P2/O3	4.40	126.6 at 0.1 C	80.6% after 200 cycles	[98]
$\text{Na}_{0.67}\text{Li}_{0.11}\text{Fe}_{0.36}\text{Mn}_{0.36}\text{Ti}_{0.17}\text{O}_2$	Element doping	P2/O3	4.20	172.0 at 1 C	85.4% after 100 cycles	[97]
$\text{Na}_{2/3}\text{Mn}_{2/3}\text{Ni}_{1/3}\text{O}_2$	Element doping	P2/O3	4.30	154.6 at 0.1 C	80.2% after 100 cycles	[99]
$\text{Na}_{0.67}\text{Mn}_{0.64}\text{Co}_{0.30}\text{Al}_{0.06}\text{O}_2$	Element doping	P2/P3	4.00	83.0 at 10 C	81% after 200 cycles	[100]
$\text{Na}_{0.66}\text{Ni}_{0.33}\text{Mn}_{0.67}\text{O}_2$	Surface coating	P2	4.30	56.4 at 12.5 C	83.7% after 100 cycles	[82]
NTP coated $\text{Na}_{0.67}\text{Co}_{0.2}\text{Mn}_{0.8}\text{O}_2$	Surface coating	P2	4.20	70.7 at 20 C	86.7% after 150 cycles	[105]
NTP coated $\text{Na}_{0.65}\text{Mn}_{0.70}\text{Ni}_{0.16}\text{Co}_{0.14}\text{O}_2$	Surface coating	P2	4.30	105.1 at 5 C	84.3% after 500 cycles	[106]
$\text{NaFeO}_2@C$	Surface coating	O3	3.40	89.6 at 0.1 C	87.3% after 100 cycles	[108]
C-PDA coated $\text{Na}_{0.80}\text{Ni}_{0.22}\text{Zn}_{0.06}\text{Mn}_{0.66}\text{O}_2$	Surface coating	P2	4.30	124.0 at 0.075 C	90.7% after 100 cycles	[109]
$\text{NaFe}_{0.5}\text{Ni}_{0.5}\text{O}_2$	Surface coating	O3	3.80	130.0	86% after 50 cycles	[111]
$\text{Na}_{0.67}\text{Fe}_{0.5}\text{Mn}_{0.5}\text{O}_2$	Surface coating	P2	4.30	190.0	38.6% after 500 cycles	[112]
$\text{NaMn}_{0.33}\text{Fe}_{0.33}\text{Ni}_{0.33}\text{O}_2$	Surface coating	O3	4.20	124.0 at 1 C	71.0% after 100 cycles	[117]
$\text{Na}_{0.8}\text{Ni}_{0.5}\text{Co}_{0.2}\text{Mn}_{0.3}\text{O}_2$	Surface coating	O3/O'3-P2	4.00	146.0 at 0.1 C	75.0% after 200 cycles	[118]
$\text{Na}_{0.67}\text{Ni}_{0.2}\text{Co}_{0.2}\text{Mn}_{0.6}\text{O}_2$	Structure architecture	P2	4.30	132.2 at 0.2 C	83.0% after 200 cycles	[123]
$\text{Na}_{0.76}\text{Cu}_{0.22}\text{Fe}_{0.30}\text{Mn}_{0.48}\text{O}_2$	Structure architecture	P2	4.00	154.1 at 0.1 C	79.0% after 300 cycles	[124]
$\text{Na}_{2/3}\text{Ni}_{1/3}\text{Mn}_{2/3}\text{O}_2$	Structure architecture	P2	3.70	84.3 at 0.2 C	83.3% after 500 cycles	[125]
$\text{NaNi}_{0.5}\text{Mn}_{0.5}\text{O}_2$	Structure architecture	O3	4.00	125.0 at 0.15 C	70.0% after 500 cycles	[126]

cutoff voltage and maintaining a sufficient capacity when considering cation doping as a strategy for improving the electrochemical performance of layered oxides. This involves optimizing the dopant concentration and selection of the dopant cation to minimize the negative impact on the capacity while still benefiting from the improved voltage stability.

Introducing high electronegative elements in layered oxides not only suppresses the Jahn-Teller effect of Mn but also activates reversible redox potential. For instance, Hu et al.^[85] adopted an F⁻ ion doped P2-type Na_{0.6}Mg_{0.3}Mn_{0.7}O₂ (NMMOF) cathode, in which F⁻ ions partially substituted O²⁻ ions. The XRD patterns confirm that dopant F⁻ plays a role in influencing the

interlayer spacing (Figure 5a) and lattice parameter (Figure 5b,c). The study revealed that the incorporation of F⁻ ions in a content of 0.05 resulted in the maximum increase in interlayer distance, indicating Mn⁴⁺ is reduced to Mn³⁺ with a larger radius and more facile Na⁺ diffusion kinetics. Besides, the formed Mn-F bond can hinder the dissolution of Mn ions and thus effectively alleviate the Jahn-Teller distortion. Besides single fluorine doping, Cui et al.^[86] designed a dual doping strategy on Na_{0.67}Ni_{0.15}Fe_{0.2}Mn_{0.65}F_{0.05}O_{1.95} by doping both F ions and Mg ions. The doping of F ions suppresses the Jahn-Teller effect and activated multiple redox potentials. Simultaneously, the substitution of Mg for Na sites results in

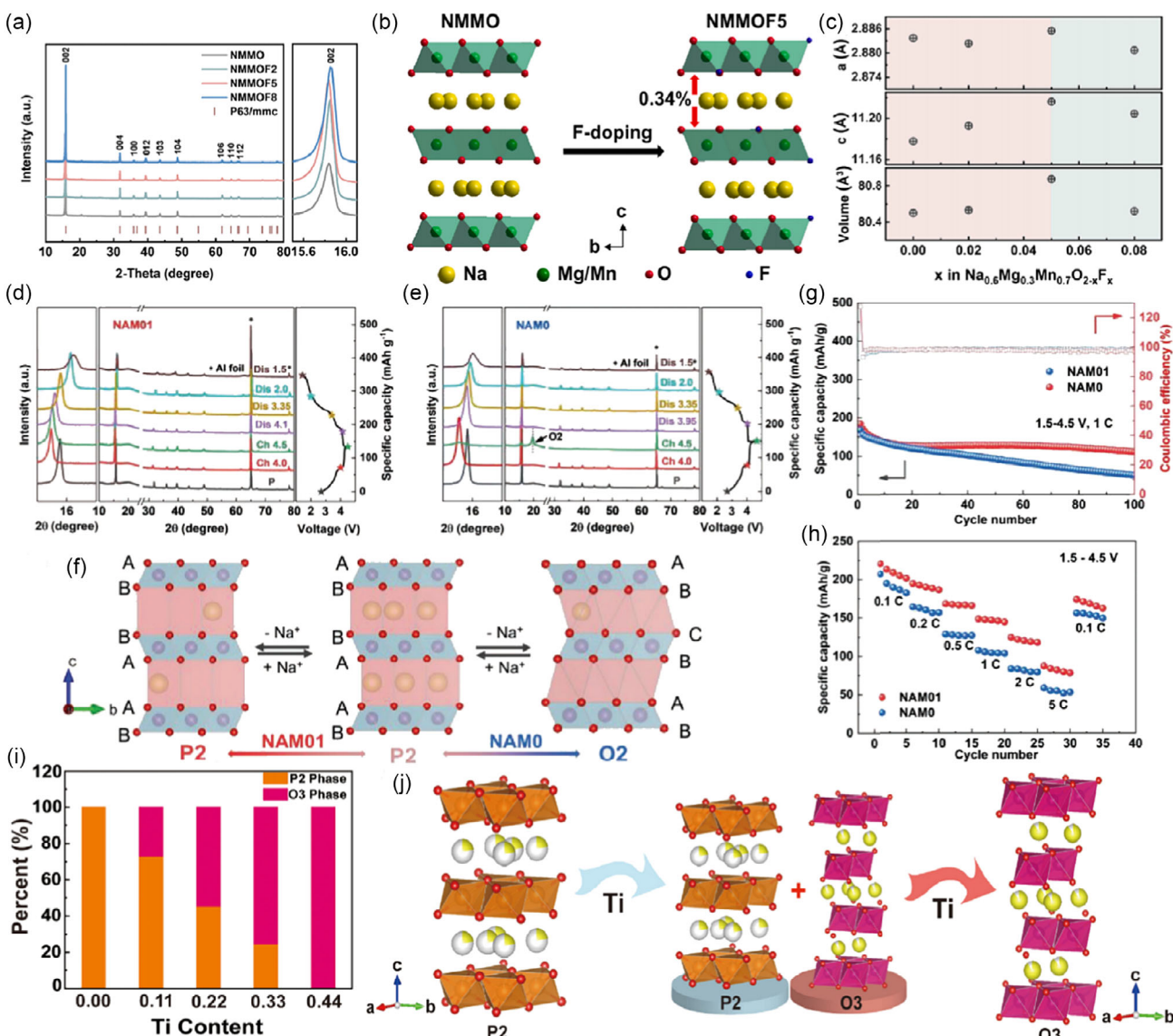


Figure 5. a) XRD patterns of NMMO cathodes with different content of F⁻ with an enlarged view of (002) diffraction peak. b) Schematic illustration of structures of NMMO and NMMOF5. c) The refined lattice parameters of NMMO with different content of F⁻. Reproduced with permission.^[85] Copyright 2022, Elsevier. d) XRD pattern of structural evolution of NAM01 and e) NAM0 electrodes during the first cycle. f) Crystal structures of NAM01 and NAM0. g) Cycling performance and h) rate capability of NAM01 and NAM0. Reproduced with permission.^[81] Copyright 2022, Wiley-VCH. i) Phase proportion of $\text{Na}_{0.85}\text{Ni}_{0.34}\text{Mn}_{0.66-x}\text{TixO}_2$ at different Ti content. j) Phase transition process with increasing Ti content of $\text{Na}_{0.85}\text{Ni}_{0.34}\text{Mn}_{0.66-x}\text{TixO}_2$ material. Reproduced with permission.^[98] Copyright 2022, Elsevier.

the formation of Mg–Mg dimers within the Na⁺ layer, coexisting with transition metals. These Mg–Mg dimers act as a pillar, expanding the Na⁺ diffusion pathway and contributing to improved electrochemical performance (Table 2).

In addition, inducing a transition metal with strong repulsion toward Na sites is also an effective modification to broaden the output voltage window. Wang et al.^[87] synthesized an Sb⁵⁺ doped P2-Na_{0.67}Mn_{0.66}Ni_{0.33}O₂ cathode material, providing an excellent electrochemical performance (Table 2). The doping of Sb⁵⁺ disrupted the ordering of Na⁺/vacancy, Mn, and Ni cations due to the induction of additional electron holes by Sb⁵⁺, which enables to adjust of the ratio of Na_e and Na_f (sites below transition metal ions and sites below oxygen ions along the c direction, respectively), thus validly facilitate Na⁺ transfer kinetics and further optimize the electrochemical performance at high voltage conditions.

3.1.2. Activate Anionic Redox Reaction

Apart from the cation redox couple, recent anionic redox reaction has raised researchers' worldwide concern for its potential of elevating working voltages and contributions to a high-capacity cathode. Specifically, transition metals located at the right side of the periodic table have shown a propensity for inducing oxygen redox reactions. This is attributed to their ability to form strong covalent bonds with oxygen, involving orbital overlaps of TMs and oxygen.^[88–90] It is worth noting that the TM–O covalence bond is weak when only 3d transition metal is involved without 4d and 5d transition metals, causing O₂ release at high voltages.^[91] Typically, major substitution transition metals that can trigger anionic redox activity are Al, Li, Mg, Zn, Cu, Ti, Sn, and so on.^[92–95] Cheng et al.^[81] reported a Al-doped P2-type Na_{0.6}Ni_{0.3}Mn_{0.7}O₂ (NAM01) material, in which Na–Al–O configurations lead to orphaned O-2p orbital, activating oxygen redox reactions. Besides, owing to the high strength of Al–O bonds formed by doping an appropriate amount of Al, the volume expansion and TM layers gliding are effectively suppressed, further hindering the P2–O₂ phase transition during Na⁺ insertion/extraction. As shown in Figure 5d–f, the O₂ phase exists in the initial MAN0 material while not in NAM01 material during the charge/discharge process. This indicates that the Al doping effectively suppresses the formation of the O₂ phase. Moreover, the larger interlayer spacing resulting from the Al doping also facilitates Na⁺ ions diffusion kinetics, as a consequence of improved cycling performance and specific capacity. (Figure 5g,h). Chen et al.^[96] synthesized a Co-doped Na-rich O₃-type Na₂RuO₃ (NRO) cathode material to improve both anionic and cationic redox processes. On one hand, the average valence state of Na_{1/3}Ru_{2/3} is +3, which is the same as Co³⁺. Thus, Co doping not only could keep valence balanced, but also facilitate the cation redox reaction of the whole system. On the other hand, the Co³⁺ ions would locate in 3b sites within the layers between TM and Na⁺ ions, improving structure stability. Besides, both Ru 4d orbitals and Co 3d orbitals would hybridize with O-2p orbitals, and Ru–O hybridized orbitals occupy a higher energy state. The existence of a Co³⁺/Co⁴⁺ redox couple enables to make sure the oxygen oxidation process finished before full Co³⁺ oxidation, serving as a redox mediator of anionic and

cationic redox reactions. As a result, Co-doped NRO delivers a higher specific capacity within the voltage range of 1.5–4.3 V and demonstrates better cycling performance than the initial NRO material. Although anionic oxygen redox reaction can improve specific capacity extremely, there still exist some shortcomings including structural destruction caused by inevitable oxygen gas release and phase transformation. Thus, enhancing structure stability is of great importance to modify the electrochemical performance of layered oxides.

3.1.3. Enhance Structure Stability

To solve the issue of the poor stability of layered oxides without sacrificing capacity, a valid approach is to create biphasic or triphasic hybrid materials through doping modifications. Because an intersected phase boundary formed between two or three different layered phases enable to suppression of complex phase transition, alleviates inner stress, and combines their advantages. This strategy contributes to improved stability while retaining high capacity in layered oxide cathode materials. For example, by combining the superiorities of the high capacity of the O₃ phase and the fast ion diffusion kinetics of the P2 phase, the structure stability of layered oxides can be enhanced without sacrificing capacity, and in some cases, the capacity can even be increased.^[97] Recently, Yu et al.^[98] created a P2/O₃ composite Na_{0.85}Ni_{0.34}Mn_{0.33}Ti_{0.33}O₂ (NMT) material by doping a specific amount of Ti element, achieving remarkable electrochemical performance. As depicted in Figure 5i,j, Ti substitution plays a role in inducing the P2–O₃ phase transition. As the amount of Ti increases, the P2 phase gradually transforms into the O₃ phase, undergoing a highly reversible transition process of P2/O₃–P2/P3–OP4/OP2–P2/P3–P2/O₃ transitions within a voltage window of 2.2–4.4 V. In addition, the interlocking effect between the phase boundaries causes suppression of structural strain and volume change, leading to improved structure and cycling stability. This results in a capacity retention of 80.6% at 1 C after 200 cycles, indicating the excellent performance of the NMT composite material. Similarly, Chen et al.^[97] synthesized a kind of P2/O₃ biphasic Fe/Mn-based Li/Ti co-doped layered oxide Na_{0.67}Li_{0.11}Fe_{0.36}Mn_{0.36}Ti_{0.17}O₂, where Ti dopant participates in forming Mn–O–Ti–O–Fe bonds in transition metal layers, enhancing structure stability. Additionally, Li dopant activates oxygen redox reactions below 4.2 V and triggers the phase transition from P2 to O₃. Similar to other P2/O₃ composites, two different phases at the boundary enable minimize lattice distortion and volume change, achieving high capacity and cycling stability, thus delivering 172 mAh g⁻¹ in 2.0–4.2 V at 1 C, with capacity retention of 85.4% after 100 cycles (Table 2). Furthermore, many other types of biphasic composites display excellent electrochemical performances as well, such as P2/O₃-Na_{2/3}Mn_{2/3}Ni_{1/3}O₂ co-doped by Fe/Ti,^[99] P2/P3–Na_{0.67}Mn_{0.64}Co_{0.30}Al_{0.06}O₂^[100] doped by Co and so on.

3.2. Surface Coating

Surface coating is regarded as another promising method for cathode materials optimization. Because it serves as a protective layer to prevent adverse reactions between layered oxides and

substances in the air such as moisture attack and oxidation of transition metals.^[28] Additionally, surface coatings can enhance electrochemical performance by suppressing volume change, improving electron conductivity, and enhancing cycling stability. Nowadays, a variety of materials have been applied as coating materials, including carbon sources, metal oxides, polymers, and so on.^[101–104]

3.2.1. Increase Electron Conductivity

The requirement for portable and fast charging of batteries become more and more urgent for achieving commercialization. Driven by the fast-charging trend, improving Na^+ ions transport kinetics has attracted researchers' worldwide attention. Zhang's group^[105] designed a $\text{Na}_{0.67}\text{Co}_{0.2}\text{Mn}_{0.8}\text{O}_2$ (NCM) material wrapped by a NASICON-type $\text{NaTi}_2(\text{PO}_4)_3$ (NTP) nano-shell. Due to the large Na^+ diffusion channels of NASICON-type NTP, the Na^+ transport kinetics of NCM are facilitated effectively, providing good rate performance. The ohmic resistance (R_s) and charge transfer resistance (R_{ct}) are 5.48 and 26.4 Ω , respectively, which is much lower than the value of the original NCM. Besides, NTP has also been discovered to optimize the performance of P2-type $\text{Na}_{0.65}\text{Mn}_{0.70}\text{Ni}_{0.16}\text{Co}_{0.14}\text{O}_2$ (NMNCO) as well, with the same mechanism of broadening Na^+ ions diffusion channels.^[106] Carbon or carbon composite are also commonly applied as coating materials to increase electron conductivity.^[107] Xia's group^[108] synthesized a carbon-coated $\text{NaFeO}_2@\text{C}$, where carbon enhances Fe–O bonds, suppresses the release of oxygen, and expands Na slabs, resulting in improved electronic conductivity. Additionally, mechanical mixtures of carbon and polymer also play a comprehensive role in improving the electrochemical performance of SIBs cathode. Xia et al.^[109] designed a polydopamine-derived carbon surface coating (C-PDA) on P2-type $\text{Na}_{0.80}\text{Ni}_{0.22}\text{Zn}_{0.06}\text{Mn}_{0.66}\text{O}_2$, where C-PDA shell not only improved the electron conductivity but also serve as a protective layer to prevent side reactions.

However, controlling the amount and thickness of coating materials still remains a challenge in surface coating strategies.

3.2.2. Protect from Side-Reactions

Indeed, the occurrence of adverse side reactions at interphases can significantly impact the performance and lifespan of layered oxide cathode materials. These side reactions include HF attack, dissolution of transition metals, and oxidation reactions between the cathode materials and electrolyte.^[32] As mentioned above, the dissolution of active TMs is a significant factor contributing to the formation of an undesirable cathode-electrolyte interface (CEI), which serves as a barrier towards expected electrochemical reactions. For instance, the dissolution of Mn^{2+} ions can occur due to the Jahn–Teller effect caused by the presence of Mn^{3+} ions.^[29] Another concern related to the CEI is the corrosion caused by the reaction of sodium hexafluorophosphate (NaPF_6) with trace amounts of water present in the electrolyte. This reaction can generate HF, which can further corrode the cathode material and contribute to capacity fading and decreased performance.^[110] To tackle these issues, Moezz et al.^[111] generated an artificial cathode electrolyte interphase layer (ACEI) on

O3-type $\text{NaFe}_{0.5}\text{Ni}_{0.5}\text{O}_2$ (NFNO) through electrochemical predissolve, which generated an oriented physical barrier for dissolution of active TMs, electrolyte decomposition, and release of oxygen. They achieved this by forcing NFNO electrochemically to 1.6 V, through the insertion of a few Na^+ ions into the material to form a 35 nm ACEI layer (Figure 6a). Besides, Moezz et al.^[112] also attempted to form an ACEI layer on P2-type $\text{Na}_{0.67}\text{Fe}_{0.5}\text{Mn}_{0.5}\text{O}_2$ (NMFO) using additives Na_2CO_3 and NaF into the electrolyte. These additives undergo decomposition on the cathode surface during the charge/discharge process, leading to the formation of the ACEI layer. This work proves that by controlling the amount of additives, the thickness of ACEI can be controlled. Though ACEI exhibits a promising future in addressing the issue of unstable interfaces in cathode materials, its application is currently limited by the use of highly concentrated solutions, which is costly. Additionally, many other coatings can validly avoid adverse side reactions, such as carbon nanofibers,^[113] metal oxide,^[104,114] inorganic salt,^[115] bioinspired^[116] coatings, and so on.

3.2.3. Enhance Structure Stability

The surface coating could increase electron conductivity, and prevent side reactions of cathodes. Moreover, the coating acts as a protective layer that reduces the formation of cracks, exfoliation, and disintegration originating from inner stress generated by phase transition, HF corrosion, or O_2 release during the charge/discharge process.^[110]

Yu et al.^[117] synthesized a TiO_2 -coated O3- $\text{NaMn}_{0.33}\text{Fe}_{0.33}\text{Ni}_{0.33}\text{O}_2$ cathode, in which the TiO_2 shell successfully retains structural integrity and stability. It allows an entirely reversible phase transition during initial Na^+ intercalation/deintercalation, while the pure O3- $\text{NaMn}_{0.33}\text{Fe}_{0.33}\text{Ni}_{0.33}\text{O}_2$ cannot. Besides, TiO_2 -shell also increased spacing between interlayers by inducing Ti^{4+} dopant and increased roughness on the surface thus increasing the contact between electrolyte and cathode. Zhang et al.^[82] proposed a doping-integrated coating strategy on P2-type $\text{Na}_{0.66}\text{Ni}_{0.33}\text{Mn}_{0.67}\text{O}_2$. The material was coated with ZnO , which served as a protective layer to prevent electrolyte decomposition. Simultaneously, Zn^{2+} from the coating is doped into the material which enables suppression of Na^+ /vacancies ordering and thus, increases the reversibility of phase transition.

Apart from the typical surface coating, the core-shell structure is a novel method to address the structural damages induced by inner stress from large volume changes. Chen et al.^[118] designed a O3/O'3-P2 core-shell $\text{Na}_{0.8}\text{Ni}_{0.5}\text{Co}_{0.2}\text{Mn}_{0.3}\text{O}_2$ composite, the core material has an O3/O'3-type structure, while the shell material has a P2-type structure (shown in Figure 6b). Due to its nano-scale coherent intergrowth structure between the core and shell, the structure stability is effectively enhanced and crack propagation is prevented (Figure 6c,d). Therefore, apparent cracks were detected in O3/O'3 electrode after 50 cycles while not in O3/O'3-P2 particles. Moreover, the coherent intergrowth can relieve generated stress and inhibit volume change during the charge/discharge process (Figure 6e). Moreover, owing to its special structure, this composite possesses the superiority of large Na^+ ions diffusion channel from P2-type and high reversible capacity from O3-type, achieving better specific capacity

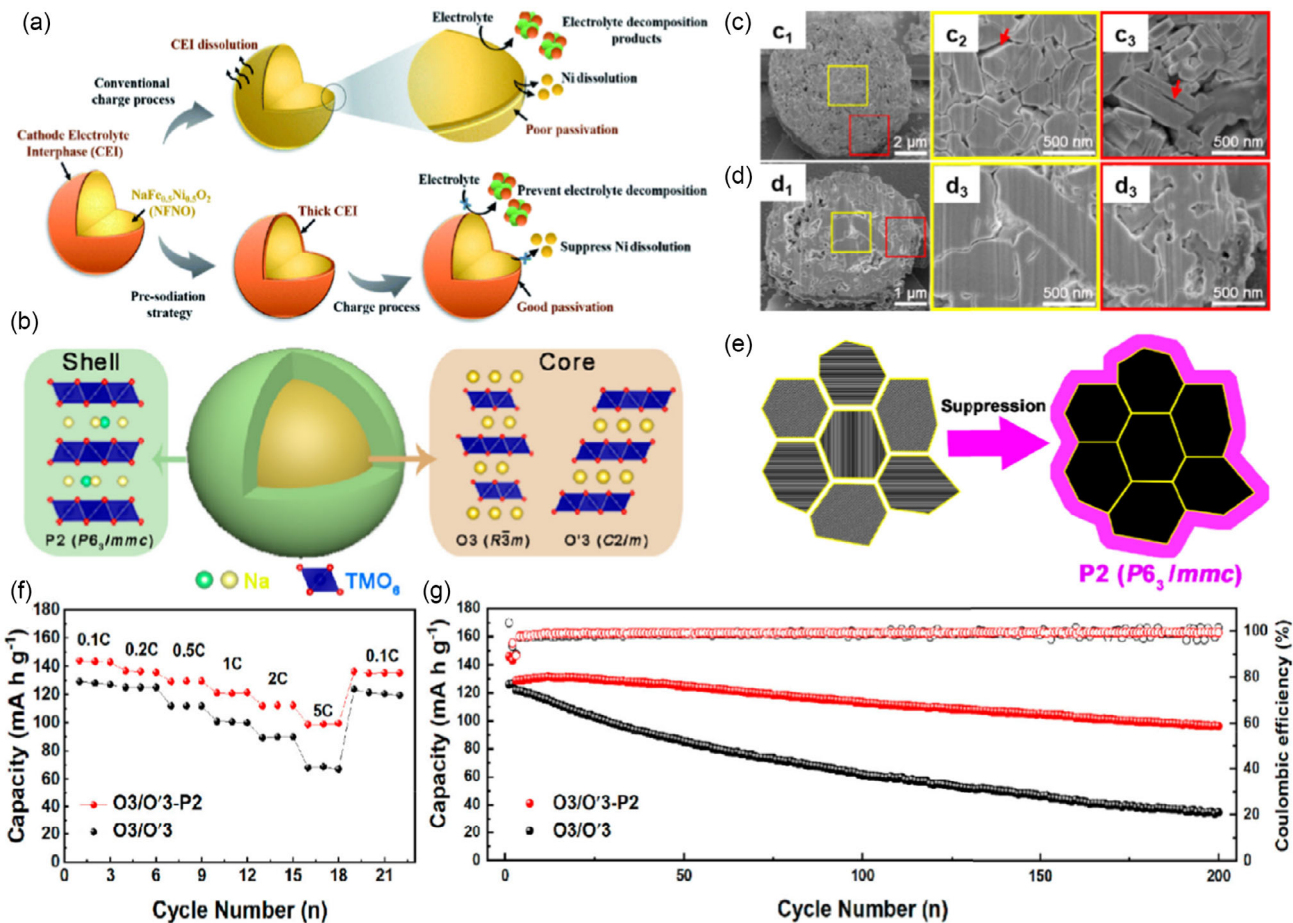


Figure 6. a) Schematic illustration of the process of the ACEI generated on $\text{NaFe}_{0.5}\text{Ni}_{0.5}\text{O}_2$. Reproduced with permission.^[111] Copyright 2020, Royal Society of Chemistry. b) Schematic illustration of core–shell structure. c) Cross-sectional SEM image after 50 cycles of the $\text{O}3/\text{O}'3$ electrode and d) $\text{O}3/\text{O}'3-\text{P}2$ electrode. e) Schematic illustration of crack suppression in the $\text{O}3/\text{O}'3-\text{P}2$ cathode. f) Rate performance and g) cycling performance of $\text{O}3/\text{O}'3$ and $\text{O}3/\text{O}'3-\text{P}2$ electrode materials. Reproduced with permission.^[118] Copyright 2020, American Chemical Society.

and cycling performance compared to the $\text{O}3/\text{O}'3$ cathode (Figure 6f,g).

3.3. Structure Architecture

It has been widely acknowledged that layered oxides with a classic structure are inadequate to meet the requirements of a high-performance SIB. Consequently, there has been a growing interest among researchers in exploring novel structure architectures to further enhance electrochemical performance. For instance, adjusting the particle size, and designing hollow, nano, or other special structures.^[119–122]

Zhang's group^[123] reported a Co-doped P2-type $\text{Na}_{0.67}\text{Ni}_{0.2}\text{Co}_{0.2}\text{Mn}_{0.6}\text{O}_2$ (NNCM) microsphere. The microsphere structure was found to reduce the contact area between the cathode and electrolyte, which effectively prevent adverse side reactions and improve long-cycling stability. In more detail, the NNCM microspheres have a regular shape with a particle size of $1.5\ \mu\text{m}$, which is relatively small compared to the irregular morphology of NNCM. As a result, the NNCM microspheres exhibit capacity retention of 83% after 200 cycles in the voltage

region of 1.5–4.2 V. Shen et al.^[124] synthesized a Cu-doped P2- $\text{Na}_{0.76}\text{Cu}_{0.22}\text{Fe}_{0.30}\text{Mn}_{0.48}\text{O}_2$ cathode with a pearl necklace-like hierarchical nanostructure, which is fabricated by the electro-spinning method. Figure 7a exhibits that Cu, Fe, and Mn are distributed randomly in the TMO_2 layer, and Figure 7b,c display that the constant nanofibers are weaved into a 3D network. In this way, the nano-necklace-like structure composed of tightly stringed nanograins possesses a large specific area adhered by myriads of active sites to react with electrolyte, it plays a crucial role in reducing the diffusion distance for Na^+ ions and enhancing electron transfer kinetics. Meanwhile, Cu dopant enables to disruption of $\text{Na}^+/\text{vacancies}$ ordering, thereby keeping constant structure during the charge/discharge process. This is confirmed by the XRD results shown in Figure 7d, the P2-type structure is well maintained over the insertion/extraction of Na^+ . The DFT calculations shown in Figure 7e,f demonstrate that Cu doping can optimize the migration path of Na ions, making it more facile and reducing the energy barrier for migration. As a result, this material gains excellent rate performance and structure stability (Table 2). The hollow structure is favorable for its abundant active sites and short ion diffusion channel. Liang et al.^[125] designed a

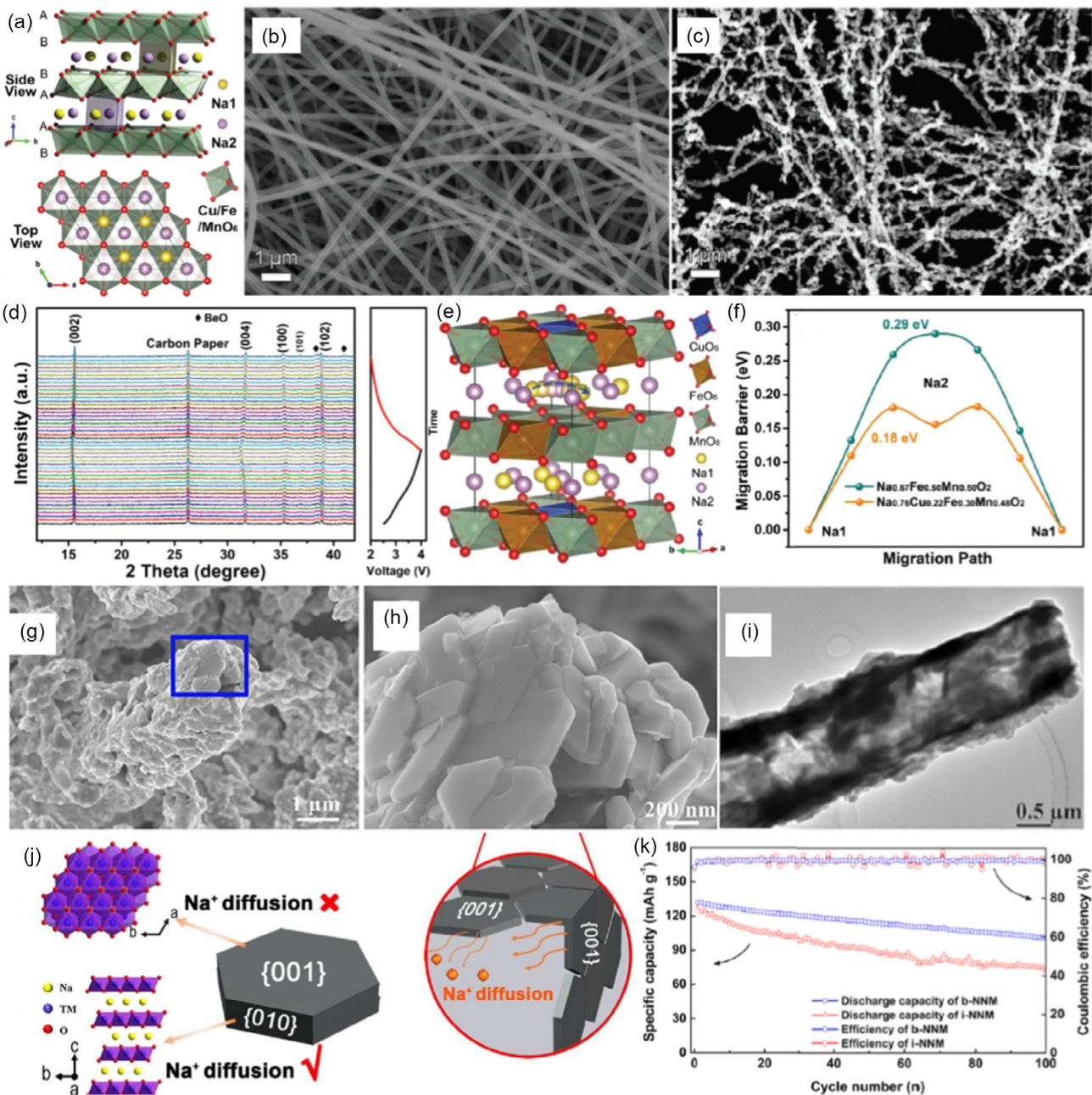


Figure 7. a) Schematic illustration of the crystal structure of $\text{Na}_0.76\text{Cu}_{0.22}\text{Fe}_{0.30}\text{Mn}_{0.48}\text{O}_2$. b) SEM images of electrospun nanofibers and c) resultant $\text{Na}_0.76\text{Cu}_{0.22}\text{Fe}_{0.30}\text{Mn}_{0.48}\text{O}_2$ nano-necklaces. d) In situ XRD patterns of $\text{Na}_0.76\text{Cu}_{0.22}\text{Fe}_{0.30}\text{Mn}_{0.48}\text{O}_2$ electrode during the first charge/discharge process at 0.1 C. e) Optimized Na ions diffusion pathway of $\text{Na}_0.76\text{Cu}_{0.22}\text{Fe}_{0.30}\text{Mn}_{0.48}\text{O}_2$ cathode after Cu doping and f) corresponding migration energy barriers of $\text{Na}_0.76\text{Cu}_{0.22}\text{Fe}_{0.30}\text{Mn}_{0.48}\text{O}_2$ and $\text{Na}_{2/3}\text{Fe}_{1/2}\text{Mn}_{1/2}\text{O}_2$ cathodes. Reproduced with permission.^[141] Copyright 2020, Wiley-VCH. g,h) SEM images of NNM at different magnifications and i) TEM images of NNM. j) Illustration of {001} and {010} faces on NNM. k) Cycling performance of i-NNM and b-NNM electrodes after 100 cycles at 0.15 C. Reproduced with permission.^[126] Copyright 2020, Elsevier.

hierarchical P2- $\text{Na}_{2/3}\text{Ni}_{1/3}\text{Mn}_{2/3}\text{O}_2$ hollow microspheres composed of nanosheets, and the hollow structure proved to be beneficial due to its abundance of active sites and short ion diffusion channels. Consequently, the hollow design increased the number of active sites, mitigated volume changes during charge/discharge, and reduced the distance for Na^+ ion diffusion, resulting in a significant improvement in the rate

performance of the material (Table 2). Mao et al.^[126] synthesized an O3-type $\text{NaNi}_{0.5}\text{Mn}_{0.5}\text{O}_2$ (NNM) hollow microbar cathode with exposed {010} facets, which were found to be electrochemically active planes for Na^+ migration compared to the {001} facets that may hinder chemical reactions (Figure 7j). The SEM and TEM images in Figure 7g–i show that the microbar is a hollow structure and is composed of various oriented

nanoparticles. Benefiting from the synergistic functions of exposure facets and hollow architecture, this electrode not only exhibited a fascinating rate performance but also achieved excellent cycling stability. As exhibited in Figure 7k, after 100 cycles the capacity retention of b-NNM is much higher than that of i-NNM. However, it should be noted that the hollow structure may lead to a decrease in energy density. Therefore, it is essential to strike a balance between energy density and electrochemical performance.^[119]

4. Optimize Strategies for Polyanionic Material Cathode

As mentioned earlier, polyanionic materials present relatively high redox potentials superior cycling and structure stability due to the inductive effect of polyanionic groups and rigid structural framework. However, their electrochemical performance is hindered by low electron conductivity and specific capacity, primarily due to the high molar mass and absence of direct electron delocalization.^[34,42,127–129] Recently, various strategies have been introduced to alleviate the shortcomings, in the aspect of element doping, improving synthetic methods, and structural and surface architecture.

4.1. Element Doping

Doping in polyanionic materials is primarily aimed at addressing the inherent issue of intrinsic low electron conductivity. It could be classified as cation doping and anion doping. Cation doping involves the substitution of Na^+ sites, polyanion sites, and transition metal (TM) sites, playing a role in enlarging the Na^+ diffusion channel, generating holes, and tuning the bandgap. In terms of anion doping, the aim is to strengthen the inductive effect.^[130] By the way, two families of polyanionic materials are mainly researched for their electrochemical performance, one is NASICON-type $\text{Na}_3\text{V}_2(\text{PO}_4)_3$ ^[131–133] and the other is vanadium-based fluorophosphate $\text{Na}_3\text{V}_2\text{O}_{2x}(\text{PO}_4)_2\text{F}_{3-2x}$.^[130,134,135]

4.1.1. Cation Doping

For $\text{Na}_3\text{V}_2(\text{PO}_4)_3$, Liu et al.^[136] designed a Fe-doped $\text{Na}_3\text{V}_2(\text{PO}_4)_3@\text{C}$ (NVFP) cathode. In this material, Fe ions were introduced by substituting partial V ions, as it exhibited the smallest formation energy for Fe doping into the V site (Figure 8b). As shown in Figure 8c, Fe doping effectively reduces the energy of the bandgap, thus facilitating the Na^+ diffusion kinetics. Moreover, because of different spin configurations of 3d orbital between Fe and V, Fe doping also enhanced the strength of V–O and P–O bonds. Besides, Fe doping can catalyze the graphitization of coated carbon, introducing more holes on the surface and then enlarging the contact area between the cathode and electrolyte (Figure 8a). Finally, the NASICON-type NVFP displayed an excellent rate capability, as the discharging rate increased from 0.1 C to 20 C, it experienced only a 21.26 mA h g⁻¹ capacity decay (Table 3). Cr doping also has been demonstrated as a beneficial method for improving electron conductivity. Yu et al.^[137] synthesized a Cr-doped $\text{Na}_3\text{V}_2(\text{PO}_4)_3$

(NVCP) cathode by using a V/Cr solid solution, which was further embedded in a dual-carbon network ($\text{V}_4\text{C}_3\text{T}_x$ and $\text{V}_3\text{CrC}_3\text{T}_x$ Mxene). The structure of NVCP@dual-carbon is illustrated in Figure 8d. As depicted in Figure 8e, Cr substitution mitigates Na^+ /vacancies ordering and forms CrO_6 octahedrons to provide a smoother diffusion path for Na^+ migration during the charge/discharge process. Cr substitution facilitates the Na^+ transfer kinetics with an improvement of 2–3 orders of magnitude higher than that of NVP. Consequently, NVCP displays higher specific capacity at a wider voltage window and better cycling stability compared to those NVP, which possesses a capacity of 78 mA g⁻¹ at 200 C (Table 3). A bimetal substitution is suitable to be applied in NVP as well for it is effective in reducing costive vanadium consumption and improving electrochemical performance. Chen et al.^[138] optimized $\text{Na}_3\text{V}_2(\text{PO}_4)_3$ by doping Co^{2+} , and Cu^{2+} ions to substitute V^{3+} , resulting in tuning the occupancy of Na^+ sites and modifying the lattice parameter, which leads to enhanced structural stability and long cycle life. Zhao et al.^[139] select Fe and Ni elements to partially substitute V in $\text{Na}_3\text{Fe}_{0.8}\text{VN}_{0.2}(\text{PO}_4)_3$ (NFVNP), It is worth mentioning that bimetal doping helps make V maintain a trivalent state and further results in high stability of NFVNP in air. Additionally, Ni substitution has an impact on increasing the capacity and lowering R_{ct} . Consequently, NFVNP exhibits an amazing power density of 6500 W kg⁻¹, 79.3 mAh g⁻¹ at 20 C, and superior cycling stability with capacity retention of 84.6% after 1400 cycles (Table 3).

As for vanadium-based fluorophosphate $\text{Na}_3\text{V}_2(\text{PO}_4)_2\text{F}_3$ (NVPF), Guo et al.^[140] synthesized a Zr-doped NVPF coated by an N-doped carbon layer. The partial substitution of V with Zr has a beneficial impact on Na^+ transfer kinetics due to a larger interplanar space. Additionally, the N-doped carbon coating layer contributes to reducing the inner resistance. As a result, NVPF-Zr-0.02/NC composite finally reaches a reversible capacity of 119.2 mAh g⁻¹ at 0.5 C and a Coulombic efficiency of 78%, which is much higher than those of NVPF. Gu et al.^[141] pioneeringly adopted a high-entropy strategy on NVPF by doping a small amount of Ca, Mg, Al, Cr, Mn elements to form a $\text{Na}_3\text{V}_{1.9}(\text{Ca}, \text{Mg}, \text{Al}, \text{Cr}, \text{Mn})_{0.1}(\text{PO}_4)_2\text{F}_3$ composite (HE-NVPF). This approach constructs a robust 3D open channel framework and effectively increases the cell parameter due to the various ionic radius of doping ions. High-entropy elements doping not only greatly enhanced the electron conductivity by decreasing the Na^+ migration energy (Figure 8h) but also increased the proportion of Na_2 sites to improve the working voltages, thus suppressing complex phase transition at high voltage. As shown in Figure 8f,g, in situ XRD patterns display that phase transition occurs in the primitive NVPF (p-NVPF) during the charge/discharge process while not in HE-NVPF. As a result, the HE-NVPF obtains excellent electrochemical performance of 445 Wh kg⁻¹ energy density and capacity retention of 80.4% after 2000 cycles at 20 C, surpassing that of p-NVPF (Figure 8i).

In addition to research on NVP and NVPF, doping modifications on other polyanionic materials have been reported recently as well. For instance, Xiong et al.^[142] proposed a Mg-doped $\text{Na}_4\text{Fe}_3(\text{PO}_4)_2(\text{P}_2\text{O}_7)/\text{C}$ (NFPP/C) composite. The Mg doping enhanced the diffusion kinetics of Na^+ ions and reduced the inner resistance, ultimately exhibiting a high rate performance

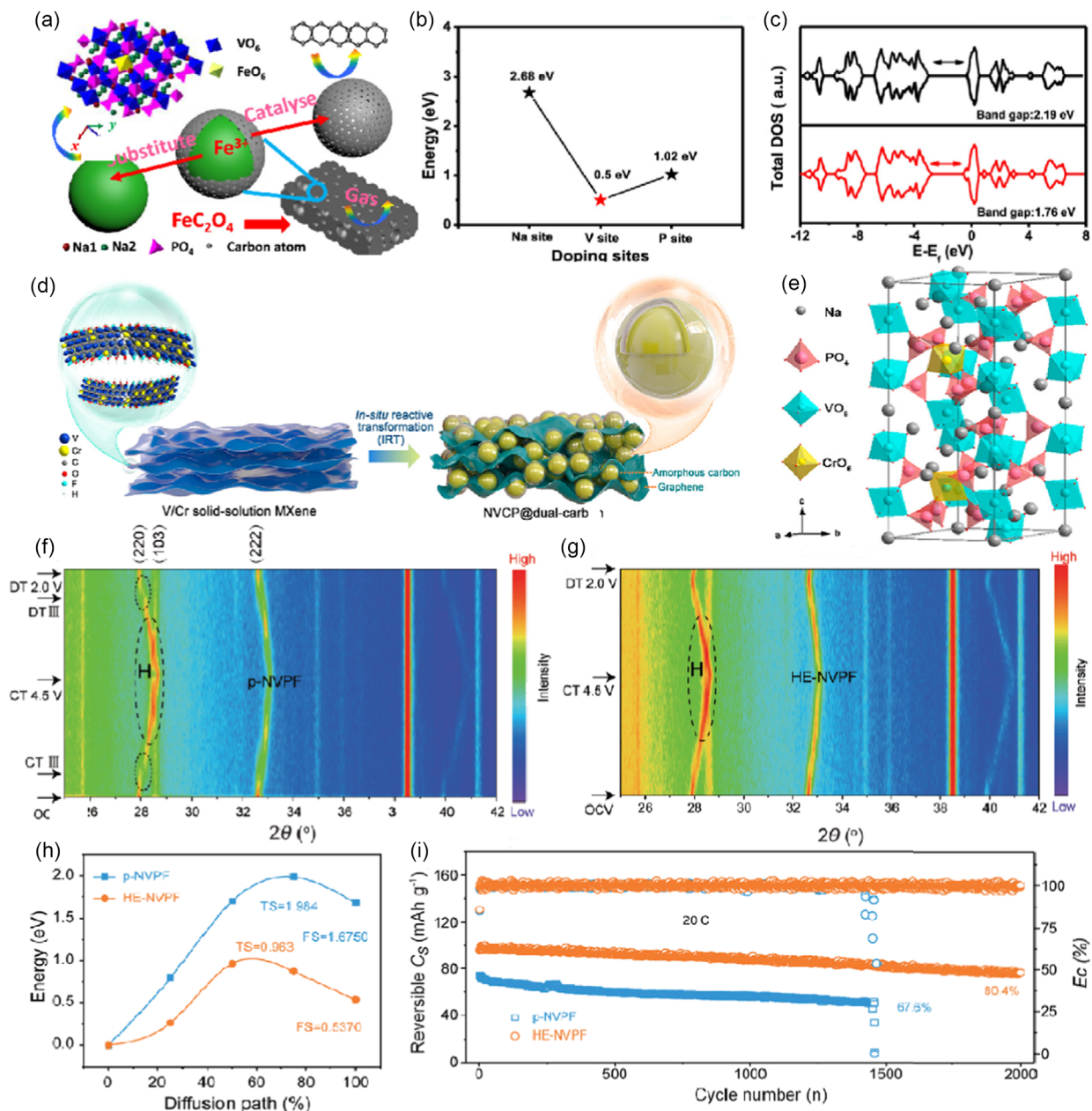


Figure 8. a) Schematic illustration of the function of Fe in $\text{Na}_3\text{V}_2(\text{PO}_4)_3@\text{C}$. b) Forming energy of Fe at different sites and c) bandgap energies of NVFP0 and NVFP15. Reproduced with permission.^[136] Copyright 2019, American Chemical Society. d) Schematic illustration of NVCP@dual-carbon architecture. e) Crystal structure and different diffusion path of Na^+ . Reproduced with permission.^[137] Copyright 2022, American Chemical Society. f) In situ XRD patterns during cycling in the voltage window of 2.0–4.5 V of p-NVPF and g) HE-NVPF. h) The migration energy profile of p-NVPF and HE-NVPF cathode material. i) Cycling performance of HE-NVPF at 0.5 and 20 C. Reproduced with permission.^[141] Copyright 2022, Wiley-VCH.

of 40 mAh g^{-1} at 20 A g^{-1} and ultralong cycling life of 14 000 cycles at 5 A g^{-1} (Table 3). Liu et al.^[143] synthesized an Al-doped $\text{Na}_4\text{Co}_3(\text{PO}_4)_2\text{P}_2\text{O}_7$ (NCPP) cathode where Al partially substitute the Co element, regulating the structure and improving ionic conductivity. It must be said that V is contained in the most popular polyanionic materials, and while it is toxic and costive,^[52] future research efforts are expected to effectively reduce V consumption and explore alternative cation dopants for substitution.

4.1.2. Anion Doping

Anion doping is another method to improve the electrochemical performance of polyanionic materials by exerting a strong inductive effect induced by electronegative anions on the polyanionic cathode. This approach leads to the development of polyanionic materials with high working plateau voltages. Recently, a series of typical anion-doped polyanionic materials were researched for SIBs.

Table 3. The electrochemical performance comparison of polyanionic materials.

Cathode materials	Optimization strategy	Type	Voltage (V)	Reversible capacity [mA h g^{-1}]	Capacity retention	References
Fe-doped $\text{Na}_3\text{V}_2(\text{PO}_4)_3$	Element doping	Phosphate	4.3	103.7 at 1 C	91.5% after 1200 cycles	[136]
Cr-doped $\text{Na}_3\text{V}_2(\text{PO}_4)_3$	Element doping	Phosphate	4.0	116 at 0.5 C	80% after 1000 cycles	[137]
Co, Cu-doped $\text{Na}_3\text{V}_2(\text{PO}_4)_3$	Element doping	Phosphate	4.0	143.3 at 0.1 C	84.7% after 50 cycles	[138]
$\text{Na}_3\text{Fe}_{0.8}\text{VN}_{0.2}(\text{PO}_4)_3$	Element doping	Phosphate	4.5	79.3 at 20 C	84.6% after 1400 cycles	[139]
Zr-doped $\text{Na}_3\text{V}_2(\text{PO}_4)_2\text{F}_3$	Element doping	Fluorophosphates	4.5	119.2 at 0.5 C	90.2% after 1000 cycles	[140]
$\text{Na}_3\text{V}_{1.9}(\text{Ca, Mg, Al, Cr, Mn})_{0.1}(\text{PO}_4)_2\text{F}_3$	Element doping	Fluorophosphates	4.3	118.5 at 0.1 C	80.4% after 2000 cycles	[141]
Mg-doped $\text{Na}_4\text{Fe}_3(\text{PO}_4)_2(\text{P}_2\text{O}_7)/\text{C}$	Element doping	Pyrophosphates	3.8	40 at 20 A g^{-1}	80.8% after 14 000 cycles	[142]
Cl-doped $\text{Na}_3\text{V}_2(\text{PO}_4)_2\text{O}_2$	Element doping	Polyphosphate	4.5	63 at 30 C	Almost 100% after 1000 cycles	[144]
F-doped $\text{Na}_{1-2x}\text{Ti}_2(\text{PO}_4)_{3-x}\text{F}_x$	Element doping	Phosphate	4.2	108.7 at 50 C	75.5% after 2000 cycles	[145]
Br-doped $\text{Na}_3\text{V}_2(\text{PO}_4)_2\text{F}_3/\text{C}$	Element doping	Fluorophosphates	4.2	116.1 at 1 C	98.3% after 1000 cycles	[146]
$\text{Na}_2\text{FePO}_4\text{F}@C@MCNTs$	Structure architecture	Fluorophosphates	2.75	188.4 at 0.1 C	97% after 700 cycles	[148]
$\text{Na}_4\text{MnV}(\text{PO}_4)_3@C$	Structure architecture	Phosphate	3.8	60 at 10 C	99% after 60 cycles	[150]
$\text{Na}_3\text{V}_2(\text{PO}_4)_2\text{F}_{2.5}\text{O}_{0.5}$	Structure architecture	Fluorophosphates	4.3	84 at 10 C	86% after 2000 cycles	[160]
$\text{Na}_3\text{MnTi}(\text{PO}_4)_{2.83}\text{F}_{0.5}$	Structure architecture	Fluorophosphates	4.3	177 at 0.1 C	83% after 500 cycles	[161]
$\text{Na}_3\text{V}_2(\text{PO}_4)_3$	Structure architecture	Phosphate	3.6	61.84 at 20 C	Almost 100% after 2100 cycles	[162]
$\text{Na}_4\text{Fe}_3(\text{PO}_4)_2(\text{P}_2\text{O}_7)@\text{C}@r\text{GO}$	Surface coating	Polyphosphate	3.8	80.7 at 20 C	91.7% after 10 000 cycles	[153]
$\text{Na}_4\text{MnV}(\text{PO}_4)_3@Ce\text{O}_2/\text{C}$	Surface coating	Phosphate	3.8	91 at 5 C	86.1% after 2000 cycles	[158]
$\text{Na}_4\text{MnV}(\text{PO}_4)_3/\text{C}@C$	Surface coating	Phosphate	3.8	81.3 at 10 C	94.3% after 500 cycles	[156]
$\text{Na}_3(\text{VOPO}_4)_2\text{F}$	Synthetic modification	Fluorophosphates	4.2	142 at 0.1 C	94.5% after 100 cycles	[163]
$\text{Na}_3(\text{VOPO}_4)_2\text{F}$	Synthetic modification	Fluorophosphates	4.05	111 at 0.1 C	70% after 3000 cycles	[167]
NVPF@rGO	Synthetic modification	Fluorophosphates	4.1	91.5 at 10 C	67.0% after 3000 cycles	[168]

Wang et al.^[144] synthesized Cl-doped $\text{Na}_3\text{V}_2(\text{PO}_4)_2\text{O}_2\text{F}$ ($\text{NVPO}_{2-x}\text{Cl}_x\text{F}$) cathode, in which Cl doping makes remarkable contributions to enhancing the rate performance and cyclic stability by tuning the electron distribution and density in NVPO₂F lattice and V center. Overall, Cl doping enlarges Na^+ diffusion space and decrease the migration energy bandgap (Figure 9a,b). Finally, NVPO_{2-x}Cl_xF realizes a superior rate capacity of approximately 63 mAh g^{-1} at 30 C and better cycling performance compared to the NVPO₂F cathode (Figure 9c,d). As a highly electronegative element, fluorine is commonly employed as an anion dopant. Deng et al.^[145] created a carbon-coated F-doped $\text{Na}_{1-2x}\text{Ti}_2(\text{PO}_4)_{3-x}\text{F}_x$ (F-NTP@C) composite. The synthetic route and its basic structure are exhibited in Figure 9e. After F⁻ doping, C—F, and Ti—F bonds are constructed, leading to the modified NTP structure being changed (Figure 9f). As depicted in Figure 9g, F⁻ doping decrease the band gap, which facilitates Na^+ transfer kinetics. As a result, F-NTP@C materials achieve a capacity of 131.3 mAh g^{-1} with initial Coulombic efficiency of 94.8% and excellent rate capabilities of 123.5 to 108.7 mAh g^{-1} from 0.5 to 50 C. Hu et al.^[146] design a Br-doped $\text{Na}_3\text{V}_2(\text{PO}_4)_2\text{F}_3/\text{C}$ composite where partial F is substituted by Br. Br doping not only relieves the consumption of fluorine but also reduces charge localization and enhances electron conductivity. Additionally, Si elements also could be applied as dopants in polyanionic materials by substituting P in the polyanion group. For instance, Aragón^[147] synthesized $\text{Na}_{3+x}\text{V}_2(\text{PO}_4)_{3-x}(\text{SiO}_4)_x$ ($0 \leq x \leq 0.5$) as cathode material for SIB, in which Si doping enlarges Na^+ diffusion channels, leading

to better rate capability and cyclability compared to the Si-free sample. Generally, it is important to note that an appropriate amount of anion doping is desired to optimize the electrochemical performance. Excessive dopants can cause changes in the framework structure and degradation of capacity. Therefore, careful control of the doping level is necessary to achieve the desired electrochemical properties.

4.2. Surface Coating

Apart from element doping, surface coating is also an improved approach for enhancing electron conductivity and structural stability. Especially, among variable coating materials, carbon is the most favorable one, this is not only because carbon can serve as a coating layer but also because it can hybridize with polyanionic materials to form a strong matrix, such as carbon nanotube,^[148,149] carbon fiber,^[150–152] carbon nanosheet,^[153–155] and so on. Overall, carbon decoration strategies have been shown to strengthen structure stability, hamper particle growth, and facilitate electron conductivity.

In the work of Gao et al.,^[153] $\text{Na}_4\text{Fe}_3(\text{PO}_4)_2(\text{P}_2\text{O}_7)$ cathode material with a mesoporous sponge-like structure caged in carbon layer and cross-linked graphene nanosheets (NFPP@C@rGO) was fabricated. The dual-carbon matrix consists of a conductive framework formed by the carbon-coating layer and rGO nanosheets (Figure 10a,b), which can not only accelerate ion transfer kinetics but also suppress the volume change during the Na^+ charge/discharge process. As shown

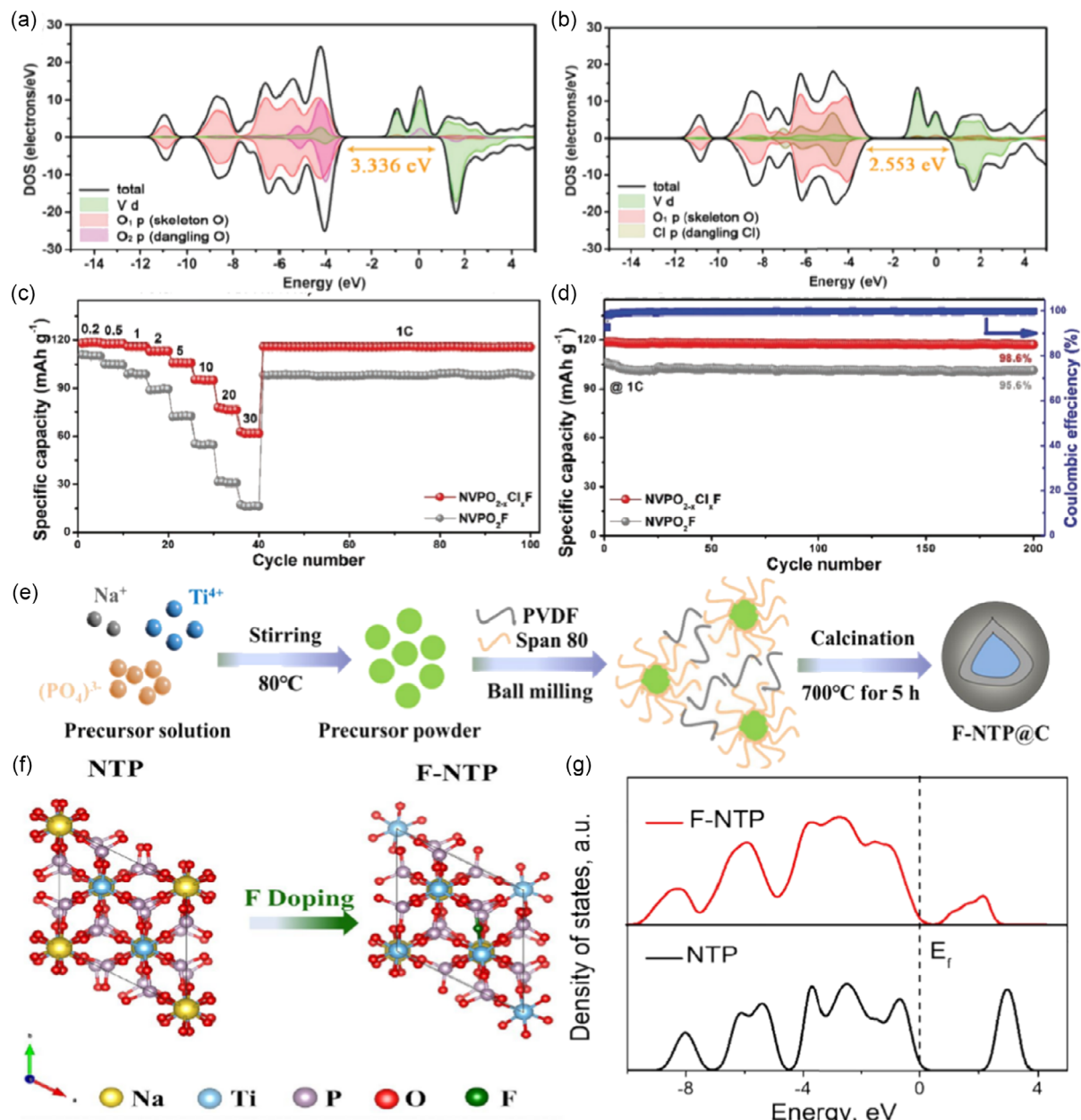


Figure 9. a) The density of states of $\text{Na}_3\text{V}_2(\text{PO}_4)_2\text{O}_2\text{F}$ and b) $\text{Na}_3\text{V}_2(\text{PO}_4)_2\text{Cl}_2\text{F}$. c) Rate performance and d) cycling performance of $\text{Na}_3\text{V}_2(\text{PO}_4)_2\text{O}_2\text{F}$ and $\text{Na}_3\text{V}_2(\text{PO}_4)_2\text{Cl}_2\text{F}$. Reproduced with permission.^[144] Copyright 2021, Wiley-VCH. e) Schematic illustration of the synthetic route of F-NTP@C. f) Structural illustration of F-NTP. g) DOS of NTP and F-NTP. Reproduced with permission.^[145] Copyright 2021, Elsevier.

in Figure 10c, there is only a 4.1% volume change after 75% Na^+ extraction. Finally, it obtains a peculiar cycling performance with a capacity retention of 91.7% over 10 000 cycles at 20 C, which is much higher than that of NFPP@C which is 26.8 % (Figure 10d). Ma et al.^[156] designed a double-carbon-layer coating strategy on $\text{Na}_3\text{V}_2(\text{PO}_4)_3$ (NMVP/C@C), which is synthesized by sol-gel method (Figure 10e). Figure 10f-i shows the TEM and HRTEM images of NMVP/C and NMVP/C@C, highlighting the distinct micromorphology of these two cathode materials. On the surface of NMVP/C@C, there is not only an amorphous

individual carbon layer similar to NMVP/C but also a carbon film carbon layer. The double carbon layers as a conducting network, play a crucial role in enhancing electron conductivity, as well as protecting cathode material from corrosion and avoiding electron polarization. Consequently, the NMVP/C@C constrains the polarization and the voltage platform decay compared to NMVP/C. As shown in Figure 10j,k, the voltage platforms and redox peaks are well maintained, while NMVP/C exhibits poor structural stability and capacity. NMVP/C@C displays an excellent electrochemical performance of 80.7 mAh g⁻¹ over

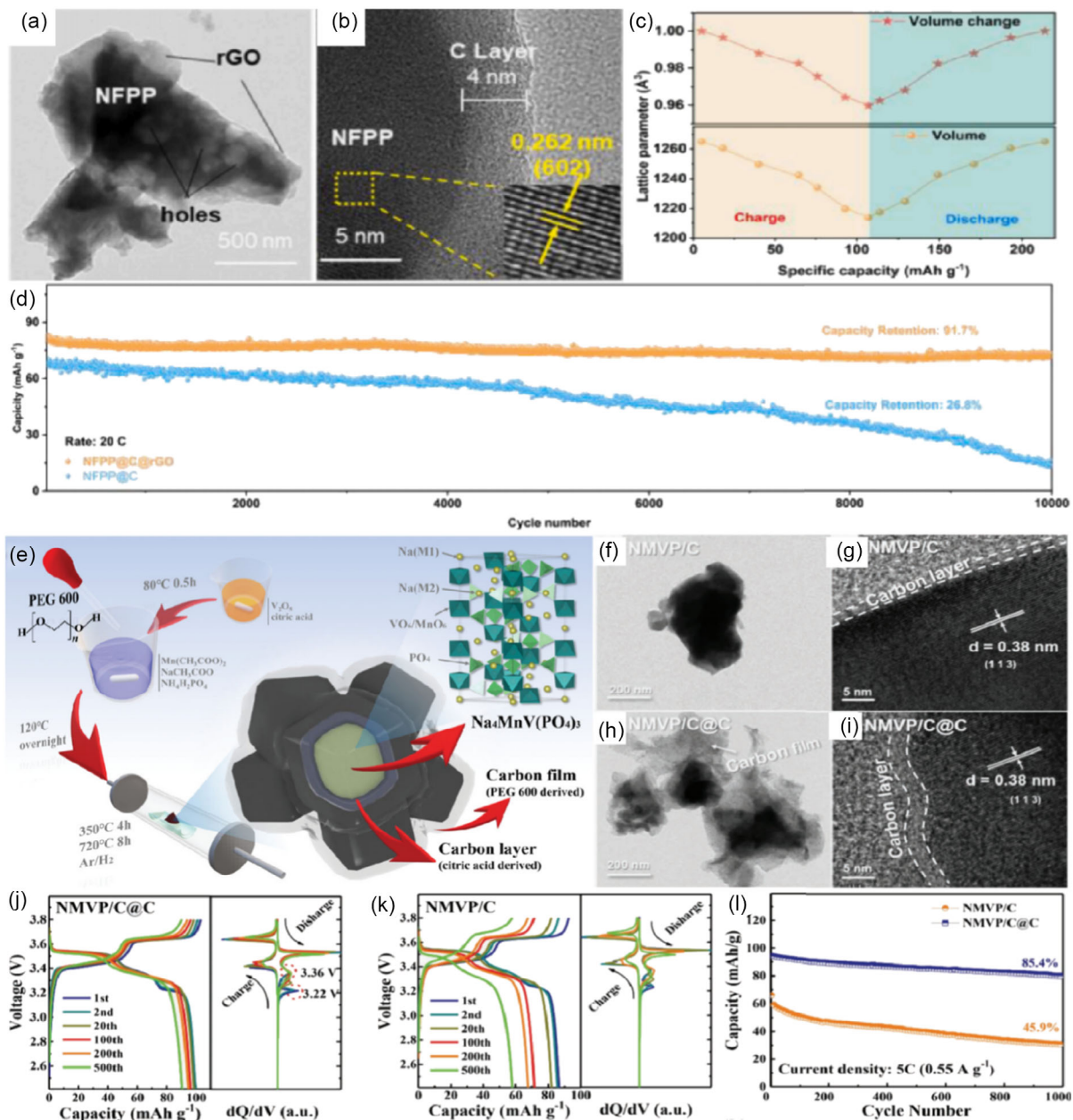


Figure 10. a) TEM and b) HRTEM images of NFPP@C@rGO. c) Volume change of NFPP@C@rGO after full charge/discharge process. d) The cycling performances of NFPP@C@rGO and NFPP@C. Reproduced with permission.^[153] Copyright 2023, Elsevier. e) Schematic illustration of the synthesis process of NMVP/C@C cathode. f) TEM and g) HRTEM images of NMVP/C cathode. h) TEM and i) HRTEM images of NMVP/C@C cathode. j) Charge/ discharge and capacity profiles at different cycles for NMVP/C@C and k) NMVP/C. l) Cycling performance of NMVP/C and NMVP/C@C at 5 C. Reproduced with permission.^[156] Copyright 2022, Wiley-VCH.

1000 cycles, with a capacity retention of 85.4% at 5 C, which is much better than that of NMVP/C (45.9%, Figure 10l). Similarly, a dual-carbon matrix composed of a carbon layer and carbon nanosheet can endow long-cycle stability. Besides, Pandit et al.^[157] proposed a carbon-coated Na₃V₂(PO₄)₃ (NVP-C) cathode with a core–shell structure synthesized by solid-state method, displaying a capacity of 104 mAh g⁻¹ at 0.1 C and an extraordinary capacity retention of 99.9% of the first cycle after 3500 cycles. Moreover, the assembled Pb//NVP-C full coin cell

exhibits a good reversible capacity of 233 mAh g⁻¹ at 0.1 C. This design provides new insight into the recycling of lead-acid batteries.

A composite of carbon and metal oxide can also be applied as a coating material, synergistically boosting the electron conductivity. Wang et al.^[158] synthesized a Ce-doped NMVP@CeO₂/C cathode material, coated by CeO₂/C composite. Owing to the larger Ce ions, the diffusion channel for Na⁺ is enlarged and the tendency of volume change for Na⁺ insertion/extraction is weakened. Moreover, CeO₂/C coating acts as a protective layer,

preventing corrosion of the cathode and contributing to the excellent cycling performance and electron conductivity of NMVP@CeO₂/C.

4.3. Structure Architecture

Structure architecture is the other valid approach to improve the electrochemical performance of polyanionic material. Though they possess a 3D open framework and high working voltage, polyanionic materials often suffer from capacity degradation and poor rate capability, which hinders their commercialization. Altering microstructure is a research hotspot to achieve improved mechanical and electrochemical performance of polyanionic cathode materials. Furthermore, integrating microstructure modification with morphology optimization is often employed for synergistic enhancement. One approach is to hybridize polyanionic particles with carbon materials to construct a complex skeleton.^[159] The following are some present studies focusing on the optimization of polyanionic cathode materials in the aspect of structure and morphology.

4.3.1. Hybrid Structure

As mentioned earlier, while polyanionic materials possess large 3D open frameworks, they often suffer from limited electron conductivity and low energy density. Simple structure architectures such as hollow and porous structures alone are insufficient to achieve the desired electrochemical performance. Therefore, combined strategies involving multiple complex structure architectures, along with carbon hybridization, coating, or element doping, have garnered significant interest worldwide.

Recently, a well-designed “internal-external” combined strategy on Na₃V₂(PO₄)₂F_{2.5}O_{0.5} composite (N-NVPFO) applied for the quasi-solid-state battery was proposed by Li et al.^[160] N-NVPFO, with its flower-like structure composed of three-dimensional nanosheets and N-doping via the solvothermal method, demonstrates superior rate capability. As displayed in Figure 11a,b, SEM images indicate that cross-linked nanosheets generate macropore architecture, which can shorten the Na⁺ diffusion distance and provide more active sites for chemical reactions. Furthermore, the surface of N-NVPFO is wrapped with a carbon layer, which synergistically improves electron conductivity. N-doping in the N-NVPFO composite serves to lower the energy gap (Figure 11c,d) and stabilize the vanadium valence state, while also leading to the generation of oxygen vacancies. Consequently, the N-NVPFO composite achieved a great rate performance of 84 mAh g⁻¹ at 10 C and capacity retention of 86% after 2000 cycles at 5 C (Table 3). Apart from the complex flower-like structure, Liu et al.^[161] designed a hierarchical and porous structure on NASICON-type Na₃MnTi(PO₄)_{2.83}F_{0.5} (NMTPF) composite by sol-gel method (Figure 11g). By introducing F⁻ to partial substitute PO₄³⁻, the particle size could be controlled via inducing effect owing to its high electronegativity, resulting in a formation of porous structure (Figure 11e,f). Similar to nanosheets, nanoparticles also effectively enable to shorten the Na⁺ diffusion distance, and the porous structure facilitates the permeation of electrolyte into the cathode material by enlarging the contact area. Disturbing the regular long-ordered crystalline

structure is another approach to enhance electron conductivity. Geng et al.^[162] synthesized a homogeneous biphasic Na₃V₂(PO₄)₃ cathode (HNVP), which is hybrid of Na₇V₄(P₂O₇)₄PO₄ (Na₇VP) and Na₃V₂(PO₄)₃ (Na₃VP). In HNVP, a section of the amorphous phase consists of nano-scale short-ranged Na₃VP and Na₇VP, where the grain boundaries are generated providing an expressway for Na⁺ ions diffusion because of the alleviation of inner stress during the Na⁺ insertion/extraction process. This, significantly facilitates the Na⁺ ions transfer kinetics, because more Na⁺ ions will be extracted from the Na₃VP component to Na₇VP in the biphasic structure (Figure 11h). As a result, HNVP//NTP full cells deliver a satisfying rate capability of 61.84 mAh g⁻¹ up to 20 C and capacity retention of 94.48% over 800 cycles at 10 °C (Figure 11i,j). This strategy also provides new insight into the potential applications of other composite materials in the future.

4.3.2. Structure Coupled with Carbonaceous Matrix

Structure coupled with carbonaceous matrix has been confirmed can strongly enhance the framework and optimize cycling performance. Recently, Su et al.^[159] designed a Na₃V₂(PO₄)₃ (NVP) nanoparticles coated by a NVP@C composite with hierarchically porous carbon skeleton. The NVP nanoparticles are anchored on the pore structure, which shortens the Na⁺ diffusion distance, facilitates the permeation of electrolytes, and alleviates the inner stress during Na⁺ insertion/diffusion. Consequently, NVP@C brings out superior rate capability and cycling stability. Additionally, hybridizing with carbon nanotubes (CNTs) also is an effective method for polyanionic material to enhance rate performance. Gao et al.^[148] synthesized a Na₂FePO₄F/carbon/multiwalled carbon nanotube microspheres (NFPF@C@MCNTs) composite, where the microsphere structure effectively mitigates volume change and enhances ion diffusion kinetics. This composite demonstrates a reversible specific capacity of 118.4 mAh g⁻¹ at 0.1 C and a capacity retention of 97% over 700 cycles (Table 3). Nanofibers, commonly constructed by electrospinning technology, possess worthy merits serving as electrode materials for the benefit of facile ion transportation, electrolyte/cathode interaction, and so on. Hu et al.^[150] synthesized a Na₄MnV(PO₄)₃@C (F-NMVP@C) fiber membrane which is used as a cathode directly without additional processing steps. Owing to the fabrication of fiber membrane, the Na⁺ transference is ultra-facilitated and morphology stability is extensively enhanced. Consequently, the F-NMVP@C demonstrates an excellent performance of 60.0 mAh g⁻¹ at 10 C and 99% capacity retention at 0.2 C after 60 cycles (Table 3).

4.4. Synthetic Methodologies

Traditional synthetic methodologies limit large-scale industrial production of polyanionic materials due to the high-temperature sintering process, resulting in the volatilization of hazardous substances and impurity generation.^[131,163–165] Moreover, elements such as vanadium and fluorine, which are extensively used, make cathode materials costive and risky at high temperatures.^[131,163–165] Thus, it is urgent to improve the synthetic methodologies. The development of designing novel

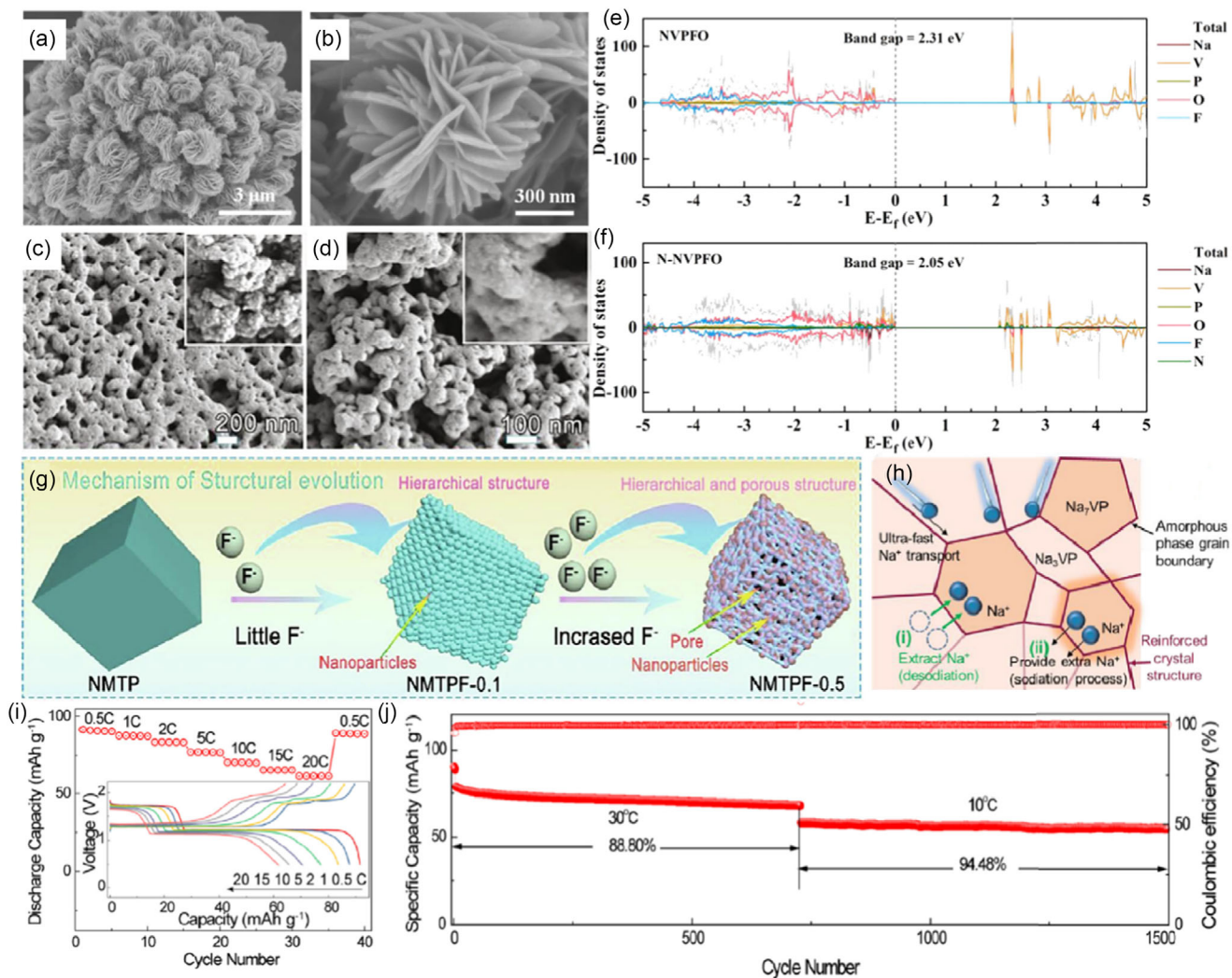


Figure 11. a,b) SEM images of N-NVPFO at different magnifications. The calculated DOS of c) NVPFO and d) N-NVPFO. Reproduced with permission.^[160] Copyright 2021, Elsevier. e,f) SEM images of NMTPF-0.5 at different magnifications. g) Schematic illustration of NMTPF structural evolution with the increasing amount of F⁻. Reproduced with permission.^[161] Copyright 2022, Elsevier. h) Illustration of Na ions diffusion on the biphasic synergy of the homogeneous hybridized HNVP. i) Rate performance and corresponding charge/discharge curves of the HNVP//NTP full cell. j) Cycling performance of HNVP//NTP full cells. Reproduced with permission.^[162] Copyright 2022, Elsevier.

synthetic methodologies not only be beneficial to tackle the issues of environmental unfriendliness but also plays a role in fabricating nano-structural polyanionic materials with accurately designed parameters in aspects of particle size, porosity, etc.^[166] In recent years, several improved synthetic methodologies have been proposed to overcome these challenges.

Shen et al.^[163] proposed a new solvent-free mechanochemical synthetic strategy for the in situ fabrication of sodium vanadium fluorophosphate Na₃(VOPO₄)₂F (NVOPF). The method relies on high-energy ball milling (HEBM) to synthesize NVPF with high efficiency. As shown in Figure 12a, different vanadium sources such as VCl₃, V(C₅H₇O₂)₃, and V₂O₃, are utilized as raw materials to obtain pure NVPF via HEBM. The peaks in powder XRD patterns (Figure 12b) indicate good nanocrystalline features and the crystal size is as small as 5 nm. The HEBM method could reach a high yield of 94% within 30 mins, providing promising

insight for synthesizing polyanionic compounds. Qi et al.^[167] proposed a simple solution-based strategy to synthesize Na₃(VOPO₄)₂F microspheres (Figure 12c), which integrates extraction separation and materials preparation at room temperature, reducing a fair degree of production cost. Through coprecipitation reaction, the multishelled NVPF microsphere is generated on in situ bubbles during the oxidation-reduction process, serving as a soft template for hollow structure formation (Figure 12d,e). No additional operations such as sintering, nano-sizing, and carbon coating are needed, so it gives a novel low-cost method for the fabrication of multishell hollow polyanionic microspheres.

In terms of optimizing synthetic strategies to boost electrochemical performance, Sun's group^[168] designed a one-step microwave-assisted hydrothermal approach to synthesize NVPF_{1+2x}, offering a low-cost and homogeneous heating

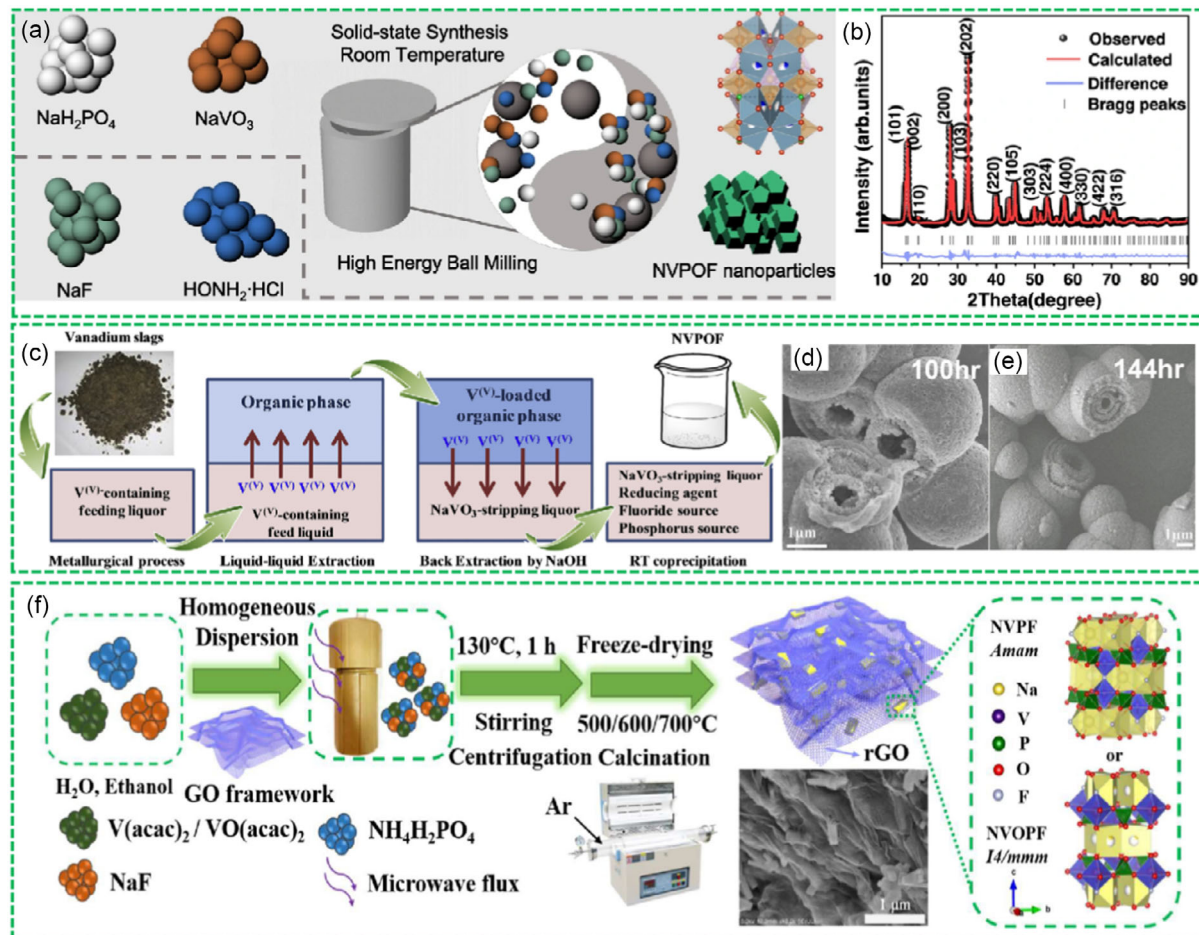


Figure 12. a) Schematic illustration of the typical synthetic process of NVOPFs. b) Rietveld-refined profiles of as-synthesized NVOPF. Reproduced under the terms of a Creative Commons Attribution 4.0 International License.^[163] Copyright 2021, Shen et al. Published by Springer Nature. c) Schematic illustration of the synthesis of NVPOF. d,e) SEM images of NVPOF microspheres at different reaction times. Reproduced with permission.^[167] Copyright 2018, Elsevier. f) Schematic synthesis approach of NVPF_{1+2x} cathodes. Reproduced with permission.^[168] Copyright 2021, American Chemical Society.

treatment (Figure 12f). This work investigates an appropriate calcination temperature (500, 600, and 700 °C) and integrates the graphene oxide (rGO) framework with NVPF_{1+2x} to synergistically optimize electron conductivity. Moreover, the use of the rGO framework with different calcination temperatures allows for altering the phase composition to take control of the electrochemical performance, providing new insight into synthetic strategies for accelerating ionic transfer kinetics.

In a word, novel synthetic strategies play a key role in the further development of polyanionic materials, particularly in reducing cost, optimizing electrochemical performance, and facilitating their industrial commercialization.

5. Optimization Strategies for Prussian Blue Analogues

To optimize the electrochemical performance and increase the commercial value of PBAs, several approaches have been proposed, including element doping, improved synthetic methods,

surface coating, and structure architecture. These approaches aim to address issues such as the presence of crystal water and inner vacancies in the PBA framework, which can react with battery systems and hinder the activity of redox couples, as well as the potential safety hazards associated with the release of toxic CN⁻.^[169-172] By synthesizing PBAs with low water content and vacancy-free structures, the electrochemical performance and safety of these materials can be enhanced.

5.1. Element Doping

Because PBAs are normally generated from solution, there inevitably exists a certain amount of coordinated water occupying the vacancies, which not only causes structure destruction but also hinders the Na⁺ diffusion kinetics during insertion/extraction and further weakens the electron conductivity.^[173] To solve these issues, enhancing crystallinity is a valid way. According to the research of Huang's group,^[174] high-crystallized PBAs have a long-range lattice periodicity, which provides a smooth diffusion

pathway for Na^+ migration. Partial substitution of TM s enables activating the redox-active sites and enhances crystallinity.^[54]

When inactive elements such as Ni, Cu, and Zn are used for doping in PBAs, their main role is to enhance the structural stability rather than directly participate in the redox reactions.^[173] For example, Zhou et al.^[175] substituted a few Fe ions by Ni within a hollow structure PB (PB-Ni). As shown in Figure 13a, after being immersed in NiCl_2 solution for one day, partial Fe ions in hollow structure PB (HS-PB) will be replaced by Ni ions. The obtained PB-Ni-1d with a fluff-like surface still maintains an evident boundary, according to the HRTEM and SEM results (Figure 13b,c). Ni doping effectively increases the number of active sites and suppresses volume change during Na^+ charge/discharge process, achieving satisfying cycling performance. Consequently, the PB-Ni-1d cathode delivers a long cycling performance of 800 cycles, much higher than that of HS-PB (Figure 13d). However, the amount of Ni content is supposed to be appropriate, as excessive inactive element doping can reduce the specific capacity. Zhang et al.^[176] introduced Zn ions to substitute the high-spin Fe ions in the $\text{Na}_x\text{Zn}_y\text{Fe}_{1-y}[\text{Fe}(\text{CN})_6]$ (ZnFeHCF-2), where Zn dopant plays a key role in improving reversible phase transition and reducing lattice distortion during

Na^+ insertion/extraction process. As increasing Zn content, the materials will gradually transform from the rhombohedral phase into the cubic phase, resulting in the presence of more Na^+ storage sites. As shown in Figure 13e–h, in situ XRD results display the reversible structure evolution, indicating that there is little volume change during the charge/discharge process. As a result, the ZnFeHCF-2 displays a high sodium diffusion coefficient of $1.774 \times 10^{-10} \text{ cm}^2 \text{ s}^{-1}$, which is significantly higher than that of ZnFeHCF-0 (without Zn ions). Furthermore, it demonstrates excellent cycle stability with a capacity retention of 58.5% after 2000 cycles.

In addition to inactive dopants, doping active elements such as Fe, Co, Mn, and so on^[173] could activate two redox sites of $\text{Fe}^{2+}/\text{Fe}^{3+}$ and $\text{M}^{2+}/\text{M}^{3+}$, thereby contributing to a high reversible capacity. Furthermore, doping multiple dopants containing both active and inactive elements in the N-coordinated M_A centers is also a strategy to improve electrochemical properties for the integration of their superiority. Peng et al.^[177] introduced the high-entropy (HE) concept into hexacyanoferrate and designed high-entropy metal-organic frameworks (MOFs) containing $\text{Na}_{1.41}\text{Mn}_{0.32}\text{Fe}_{0.11}\text{Co}_{0.28}\text{Ni}_{0.32}\text{Cu}_{0.32}[\text{Fe}(\text{CN})_6] \cdot 2.89 \text{ H}_2\text{O}$ (HE-HCF) composite. This composite extremely improves thermal stability,

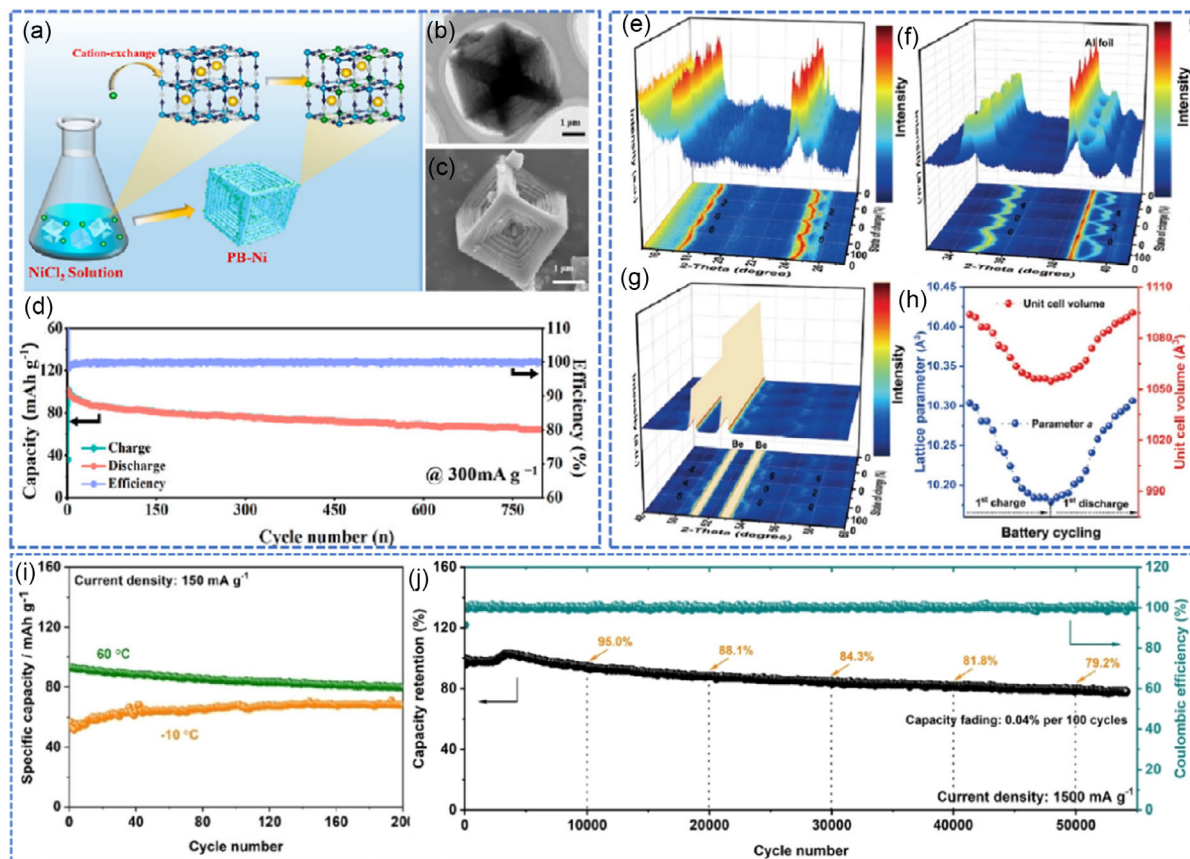


Figure 13. a) Schematic illustration of the synthesis for PB-Ni. b) HRTEM and c) SEM images of PB-Ni. d) Cycling performance of PB-Ni at 300 mA g^{-1} . Reproduced with permission.^[175] Copyright 2022, America Chemical Society. e–g) In situ, XRD enlarged the 3D colormap surface with projection and 2D contour images of ZnFeHCF-2. h) The parameter a and unit cell volume change during the first charge/discharge cycle. Reproduced with permission.^[176] Copyright 2022, Wiley-VCH. i) Cycling performance of HE-HCF at 1.5 C at different temperatures. j) Long-cycle performance of HE-HCF at 1500 mA g^{-1} . Reproduced with permission.^[177] Copyright 2022, Wiley-VCH.

structure stability, as well as specific capacity. Due to the strong diffusion kinetics of Ni, the high redox potential of Co, Mn, Fe, and the high stability of Cu, a highly reversible zero-strain two-phase Na⁺ storage system is obtained and delivers a capacity retention of 95 % after 10 000 cycles at 500 mA g⁻¹ (Figure 13j). Besides, HE-HCF exhibits peculiar stability at both high/low temperatures, indicating its tolerance to complex storage conditions (Figure 13i). By the way, apart from the M_A-site substitution, alkali-site substitution can also stabilize the structure by serving as a pillar in a pristine structure, owing to its high electrode potential.^[178–180]

5.2. Surface Coating

Surface coating is another effective approach to enhance electron conductivity, maintain structure stability, and prevent side reactions. The main coating materials are inorganics^[181–185] and conductive polymers.^[186–188] For instance, Xu et al.^[181] designed a Co_xB coating layer on MnHCF to suppress the Jahn–Teller effect of Mn. Co_xB coating not only can facilitate electron diffusion but also prevent corrosion and alleviate inner strain, thereby avoiding the formation of cracks. As a result, the Co_xB-wrapped MnHCF displays excellent structure stability and electrochemical performance (Table 4). Similarly, Liu et al.^[187] synthesized a porous Na_xFeFe(CN)₆ material wrapped by polydopamine (PDA), in which PDA tends to couple with Fe²⁺, thus enabling ion fast kinetics and enhancing the electron conductivity. Moreover, PDA also plays a role in suppressing volume change due to its good robust mechanical property, and it helps to avoid direct interaction between cathode material and electrolyte. Ye et al.^[182] adopted a chemically presodiated strategy to form a NaF-rich ACEI on the surface of PB. NaF is both an ionic conductor and electronic insulator, which can guarantee fast ion diffusion and prevent side reaction with electrolytes in the meantime. Consequently, the full cell assembled by CEI@PB cathode

and hard carbon anode exhibits an excellent cycling performance, with capacity retention of 76.3% after 2000 cycles at 1 C.

5.3. Structure Architecture

Indeed, structure modification strategies such as hollow^[189–191] and porous structures^[187,192–194] have been extensively studied to address the issues of poor electrochemical kinetics and stability in polyanionic compounds. Hollow structures provide increased Na⁺ storage sites and reduced volume change during charge/discharge cycles. They also enhance the interaction between the electrolyte and the cathode material, facilitating ion diffusion and improving overall electrochemical performance. Similarly, porous structures offer advantages such as high surface area, improved ion accessibility, and reduced diffusion path lengths, which promote efficient ion transportation and enhance the overall electrochemical performance of polyanionic materials as well. These structure architecture modifications hold great promise for the development of advanced polyanionic cathode materials for sodium-ion batteries.

Wan et al.^[191] synthesized a hierarchical cathode film composed of single-crystal PBA with a hollow cubic structure and CNTs (FeHCF nano-frames/CNTs), which is a binder-free material for high-rate SIBs. The hollow nano-cubic structure, with etched stepped sides (Figure 14a–d), significantly increases the contact area between the cathode and electrolyte. Moreover, benefitting from the fully wrapped carbon layer (Figure 14b), the PBA exhibits improved tolerance of volume change in shortened Na-ion diffusion path, thereby contributing to enhanced electronic conductivity and excellent rate capability (Table 4). Nanoflower is another noteworthy structure, which possesses unique characteristics of high stability and large contact areas. Zuo et al.^[195] demonstrated a novel-oriented self-assembly strategy to synthesize PB in a three-dimensional (3D) flowerlike structure. As depicted in Figure 14e–g, the PB flower growth is

Table 4. The electrochemical performance comparison of PBAs.

Cathode materials	Optimization strategy	Voltage [V]	Reversible capacity [mA h g ⁻¹]	Capacity retention	References
Na _{1.56} Ni _{0.32} Fe _{0.68} [Fe(CN) ₆] _{0.89} ·f _{0.11}	Element doping	3.84	114.2 at 50 mA g ⁻¹	771.4% after 400 cycles	[175]
Na _{1.55} Zn _{0.36} Fe _{0.64} [Fe(CN) ₆]	Element doping	4.2	95 at 15 mA g ⁻¹	58.5% after 2000 cycles	[176]
Na _{1.41} Mn _{0.32} Fe _{0.11} Co _{0.28} Ni _{0.32} Cu _{0.32} [Fe(CN) ₆]·2.89H ₂ O	Element doping	4.2	61 at 15 C	89.9% after 4550 cycles	[177]
Na _x Mn[Fe(CN) ₆]@Co _x B	Surface coating	4.2	Over 160 at 0.2 C	74.0% after 2500 cycles	[181]
NaFe[Fe(CN) ₆]@CNT	Surface coating	4.2	142 at 0.1 C	81% after 1000 cycles	[183]
Na _x FeFe(CN) ₆ @ZnO	Surface coating	4.2	96.6 at 500 mA g ⁻¹	57% after 500 cycles	[185]
Na _{1.36} FeFe(CN) ₆ @PDA	Surface coating	4.2	116.7 at 100 mA g ⁻¹	77.4% after 500 cycles	[187]
Na _{0.61} Fe[Fe(CN) ₆] _{0.94} ·f _{0.06} ·GO	Structure architecture	4.0	150.0 at 25 mA g ⁻¹	90.0% after 40 cycles	[184]
FeHCF nanoframes/CNTs	Structure architecture	4.2	149.2 at 0.1 C	92% after 500 cycles	[191]
Na _{1.8} Fe[Fe(CN) ₆] _{0.95} ·f _{0.05} ·2.4H ₂ O	Structure architecture	4.2	113 at 1600 mA g ⁻¹	80% after 400 cycles	[195]
K ₂ Mn[Fe(CN) ₆]	Structure architecture	4.2	120.0 at 25 mA g ⁻¹	80% after 1500 cycles	[196]
Na _{2-x} FeFe(CN) ₆	Synthetic modification	4.2	90 at 1 C	98.9% after 500 cycles	[169]
Na _{2-x} MnFe(CN) ₆	Synthetic modification	3.8	127.0 at 20 mA g ⁻¹	81.5% after 70 cycles	[197]
Na _{1.51} Fe[Fe(CN) ₆] _{0.87} ·1.83H ₂ O	Synthetic modification	4.2	124.0 at 0.1 C	59.7% after 1000 cycles	[198]
FeHCF	Synthetic modification	4.0	106.5 at 5 C	87.3% after 1000 cycles	[200]
Na _{1.46} Ni _{0.67} Fe _{0.33} [Fe(CN) ₆] _{0.87} ·1.65H ₂ O	Synthetic modification	4.0	127.9 at 10 mA g ⁻¹	93.5% after 1000 cycles	[201]

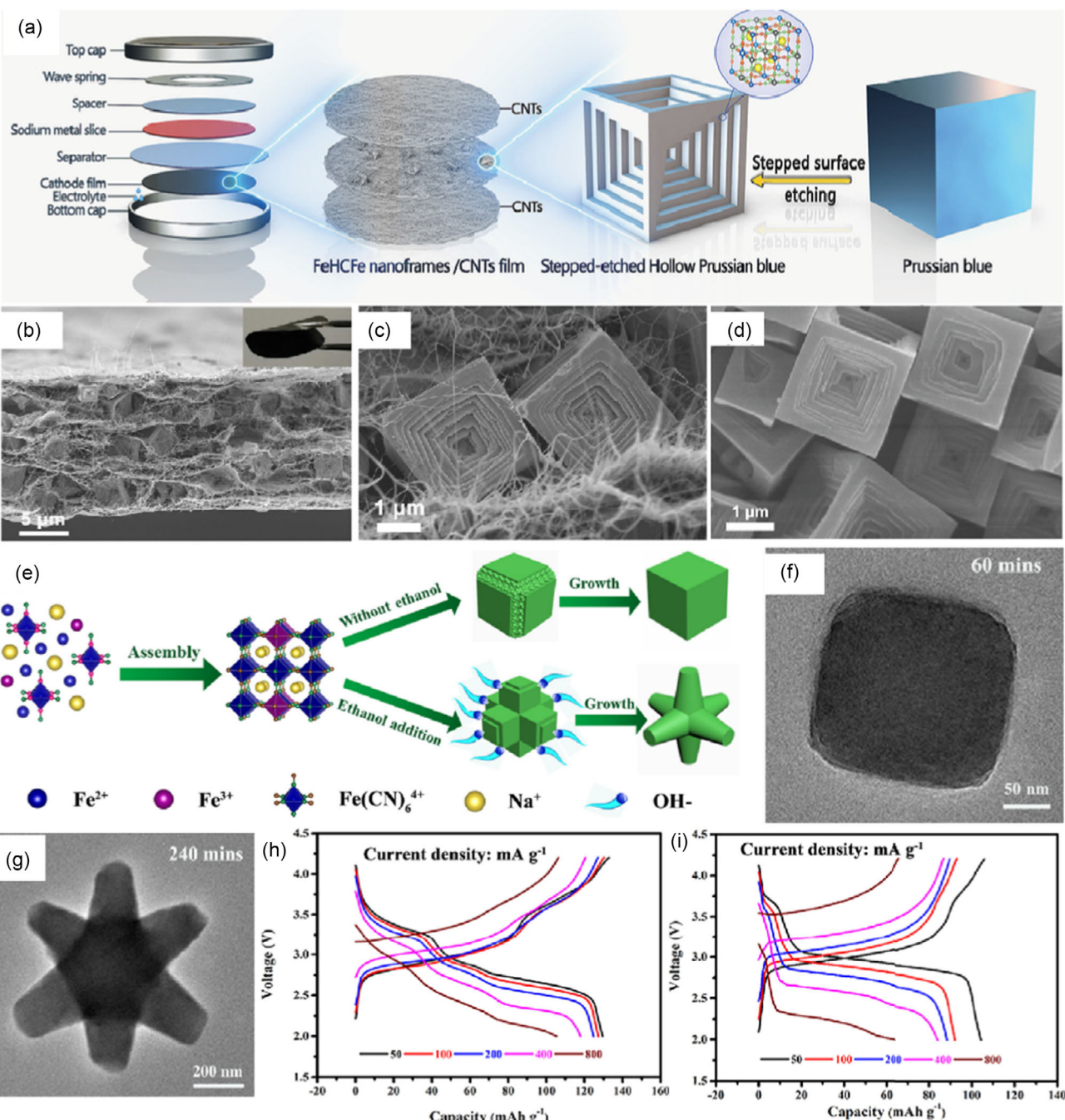


Figure 14. a) Schematic illustration of nanostructure engineering route for hollow PBA nano-frames/CNTs cathode. b) FESEM images of FeHCFe nano-frames/CNTs composites (inset: optical photo) and c) a magnified view. d) FESEM images of the corresponding stepwise hollow framework. Reproduced with permission.^[191] Copyright 2020, Wiley-VCH. e) Schematic illustration of growth mechanism for PB with cubic and flowerlike morphologies. f,g) TEM images of PB at different reaction times. h) Charge/discharge profiles of flowerlike PB electrode and i) cubelike PB electrode material. Reproduced with permission.^[195] Copyright 2020, America Chemical Society.

controlled by hydroxyl groups in ethanol, which can strongly absorb onto Fe ions and surface, inhibiting the crystal growth and thereby gaining the oriented flowerlike morphology. Consequently, this cathode material obtains high structure reversibility during transitions. Moreover, the flowerlike PB possesses minimal $\text{Fe}(\text{CN})_6^{4-}$ vacancies and large surface areas,

enabling facile ions transportation and leading to outstanding electrochemical performance. As shown in Figure 14h,i, the optimized PB displays improved specific discharge capacity and reduced polarization compared to the initial one. (Table 4). Aiming to address the adverse Jahn-Teller effect induced by the dissolution of Mn in the electrolyte, Li et al.^[196] proposed

a method to synthesize $K_2Mn[Fe(CN)_6]$ (KMF) with octahedral superstructure. This superstructure consists of submicron octahedra assembled at various angles, achieved by controlling the kinetics of topotactic transformation. By reducing the contact area between the cathode and electrolyte, this modification effectively suppresses Mn dissolution and mitigates the Jahn-Teller effect. Moreover, after several cycles of charge/discharge, partial KMF will transform into $Na_2Mn[Fe(CN)_6]$ (NMF), which suffers from stronger Jahn-Teller (JT) distortion, and the KMF can serve as a stabilizer to disrupt the long-range order of JT. Consequently, this material demonstrates ultrahigh cycling stability and excellent electrochemical performance (Table 4).

5.4. Synthetic Methods

As mentioned above, the presence of coordinated and interstitial water in PBAs synthesized from aqueous environments has negative impacts and needs to be addressed. Therefore, improving the synthetic methods becomes crucial to address this issue at its root. Wang et al.^[169] proposed a heat-treatment method to remove water from the crystal lattice of $Na_{2-x}FeFe(CN)_6$, which is placing the wet powder generated from water precipitation in a vacuum oven at 120 °C for 24 h. After heat treatment, the water is removed from the crystal lattice, accompanied by less Pauli repulsion, resulting in more compact and ordered crystals. Meanwhile, heat treatment activates low-spin Fe^{2+}/Fe^{3+} redox couples and increases the cutoff voltage to 4.2 V. Overall, heat-treated (HT) PBAs show stable cycling performance over 2000 cycles at 5 C (Table 4). Though the HT sample may absorb water again in a moist atmosphere, the electrochemical performance still be better than the pristine one. Peng et al.^[197] also designed a “water-in-salt” nanoreactor strategy, using a ball-milling synthesis process to generate a high-crystalline $Na_{2-x}MnFe(CN)_6$ composite (MnHCF) with little water content. In this strategy, no additives are involved and after 170 °C heat treatment, the obtained MnHCF exhibits stable electrochemical performance (Table 4). Additionally, Xu et al.^[198] developed a facile one-pot nonaqueous ball-milling method to synthesize a $Na_{1.51}Fe[Fe(CN)_6]_{0.87} \cdot 1.83H_2O$ material with a hollow nanosphere structure, possessing high Na content and lower defects. The detailed fabrication process and hollow structure are shown in Figure 15a–c, respectively. This hollow cathode significantly facilitates Na^+ transfer kinetics and stabilizes the crystal structure during the charge/discharge process. Notably, even at 1C, the specific capacity of this composite could reach 79.1 mAh g⁻¹ after 1000 cycles (Table 4), giving new sight into the fabrication of PBAs. By the way, the self-template method can obtain a hollow structure as well by etching the template.^[199] Overall, the three synthetic methods mentioned above share similarities as they are all facile routes for large-scale production of PBAs with low cost.

Some synthetic methods can even improve the electrochemical activation of low-spin Fe^{LS} coordinated to C atoms, effectively optimizing the specific capacity. For instance, Guo et al.^[200] used a citric acid-assisted solvothermal method to synthesize a C-FeHCF crystal, where citric acid (CA) serves as both an acid source and complexing agent, assisting in generating perfect

crystallinity with few vacancies. Additionally, CA complexes with Fe^{2+} slow down the reaction rate and prevent the oxidation of Fe^{2+} , resulting in better performance compared to the H-FeHCF synthesized by strong acid HCl (Figure 15d). From the XRD patterns (Figure 15e) and SEM results (Figure 15f), it can be observed that the C-FeHCF sample exhibits cubic structure and morphology compared to the rhombohedral structure of H-FeHCF. As displayed in Figure 15g,h, the C-FeHCF achieves an excellent electrochemical performance with an initial discharge capacity of 126.9 mAh g⁻¹ at 0.1 C and after 100 cycles, yielding a Coulombic efficiency of 99.78% (Table 4). Similarly, Shen et al.^[201] developed a disodium ethylenediaminetetraacetate (Na₂EDTA)-assisted hydrothermal method to synthesize Fe-substituted Ni-rich PBA material, in which EDTA²⁻ and Ni²⁺ reduce the rate of crystallization kinetics and activate the low-spin Fe^{LS} redox couple.

6. Challenge and Prospects

6.1. Electrochemical Performance

The electrochemical performance of layered oxides, polyanionic materials, and Prussian blue analogues has been summarized in Table 2–4, respectively. When it comes to layered oxides, two main challenges need to be addressed: the insufficient initial columbic efficiency of P2-type-layered oxides and the low structural stability of O3-type-layered oxides. As shown in Table 2, the charge/discharge cycle life for most of the layered oxides is typically in the range of hundreds of cycles, which is significantly lower compared to the cycle life of polyanionic materials and Prussian blue analogs, which can achieve thousands of cycles. The limited cycle life of layered oxides in Table 2 can be attributed to undesired phase transitions that occur during the insertion and extraction of Na^+ ions. Doping inactive elements as pillars to the framework or designing a P/O mixed-type structure can address these issues effectively but cause the scarify of capacity. As for low energy density, the key issue is the inadequate voltages. For the P2-type cathode, precharge/discharge treatment for rational sacrificial salt compensation plays a crucial role. In contrast, polyanionic materials become a hot issue because of their high energy density and stable structure framework. As summarized in Table 3, they can keep stable over thousands of cycles; however, due to the poor electron conductivity, the rate performance of polyanionic materials is insufficient. To address this issue, strategies such as enlarging Na^+ diffusion channels, controlling particle size, or coating with a conductive layer are commonly employed to accelerate the Na^+ kinetics. In PBAs, the open 3D framework offers excellent stability while excess water molecules (coordinated and interstitial water) and vacancies contained in the framework restrain the specific capacity. To optimize the performance of PBAs, researchers are exploring the use of chelating agents or surfactants to improve crystallinity. Additionally, there is a growing interest in developing solid-state synthetic strategies as an alternative to the traditional coprecipitation method in aqueous solutions. These approaches hold promise for further optimization of PBAs in terms of their electrochemical performance.

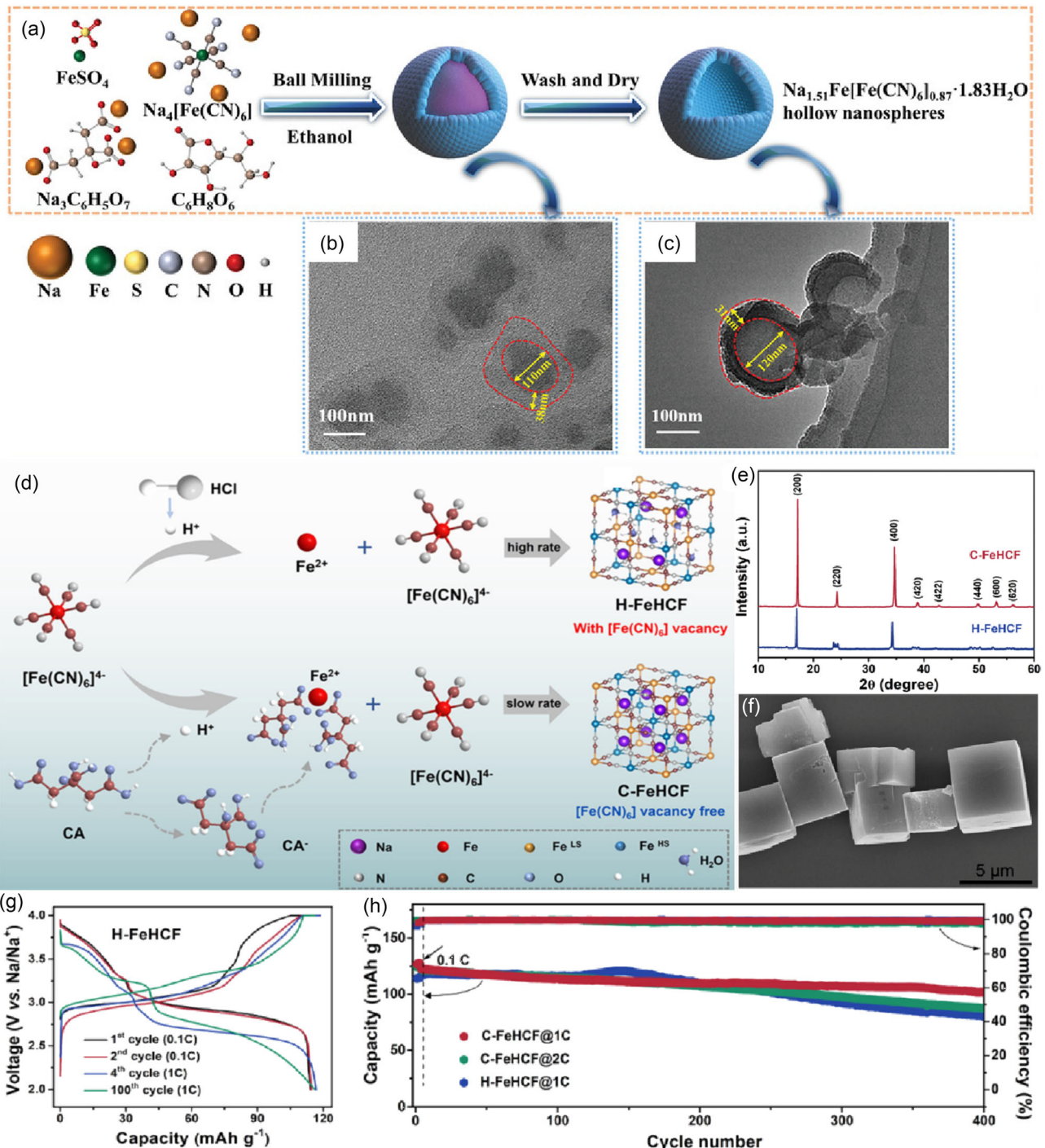


Figure 15. a) Schematic illustration of synthesis for $\text{Na}_{1.51}\text{Fe}[\text{Fe}(\text{CN})_6]_{0.87}\cdot1.83\text{H}_2\text{O}$ hollow nanospheres and b,c) corresponding SEM image. Reproduced with permission.^[198] Copyright 2022, Wiley-VCH. d) Synthesis processes of the C-FeHCF and H-FeHCF cathode materials. e) XRD patterns of the C-FeHCF and H-FeHCF cathode materials. f) SEM image of C-FeHCF cathode material. g) Galvanostatic charge/discharge profiles of C-FeHCF cathodes. h) Cycling performance of C-FeHCF and H-FeHCF cathodes. Reproduced with permission.^[191] Copyright 2023, Wiley-VCH.

6.2. Cost

To realize scaling up commercialization, researchers must take the cost of raw materials and the production process into consideration. In more detail, raw materials account for a significant

portion, approximately 80%, of the overall cost.^[202] Although sodium resources are moderate in price, other metal elements that might be used are expensive such as Co, Cr, V, Ni, and Ti. Typically, layered oxides offer more choices in terms of elemental composition, including some expensive transition metal

elements, compared to polyanionic materials and PBAs. While PBAs have a lower cost as there are almost no expensive elements existing in PBAs. In polyanionic compounds, particularly those based on vanadium, the cost is higher due to the consumption of vanadium in vanadium-based phosphates and fluorophosphate. Fe and Mn resources are readily available and cost effective. Additionally, Fe-based and Mn-based cathodes all exhibit satisfying electrochemical performance in SIBs. Therefore, by controlling the usage of expensive elements and focusing on optimizing Fe and Mn-based cathodes, particularly addressing the challenges associated with Jahn-Teller effects, significant advancements can be made toward practical industrialization of SIBs.

Furthermore, the cost of cathode production is also taken into account. For layered oxides, various synthesis methods are employed such as solid-state method, sol-gel method, and the coprecipitation method.^[203,204] Among them, the coprecipitation method is the most commonly used, undergoing the process of high-temperature calcination which is costive.^[205] Whereas, the fabrication of polyanionic materials and PBAs involves commonly a one-step synthesis method based on aqueous chemistries or mechanical methods at room temperature, showing a promising characteristic suitable for large-scale production.^[205] However, PBAs generated from aqueous chemistry may contain excess water molecules and other optimizing modifications are suggested to apply involving surface coating, carbon compositing, etc. These modifications can add to the overall cost. In terms of cost-effectiveness, the price/performance ratio for layered oxides is lower compared to polyanionic compounds and PBAs.

6.3. Environmental Impacts

Regarding environmental impacts, as mentioned above, the elements Cr and V contained in layered oxides and polyanionic are high cost and toxic. Therefore, these elements should be avoided use. In contrast, no toxic substance is involved in PBAs, but there is a concern regarding the generation of toxic and contaminative by-products such as cyanide when PBAs are decomposed at high temperatures. Moreover, raw material mining and cathode processing also have adverse environmental impacts, contributing to increasing greenhouse-gas emissions.

In terms of energy consumption, the production of layered oxides and polyanionic materials requires electricity and heat demand, which is assumed to be 6.87 kWh and 39.6 MJ kg⁻¹ of layered oxides produced, and 6.87 kWh and 15.6 MJ kg⁻¹ polyanionic compounds produced,^[202] respectively. The preparation of layered oxides will generate a certain amount of carbon emissions which are suggested to be alleviated during mass production.^[205] As mentioned earlier, although high-temperature treatments are unnecessary in the fabrication of PBAs, they also harm the environment due to the massive wastewater generation containing harmful chemical additives like chelating agents and surfactants.^[54] Despite a series of effluent treatments that have been carried out before discharge, there still exists residue.

In a word, these three materials display distinct characteristics in terms of electrochemical performance, cost, and environmental impact, and the radar chart in **Figure 16** provides a visual comparison. Layered oxides demonstrate high capacity but come with

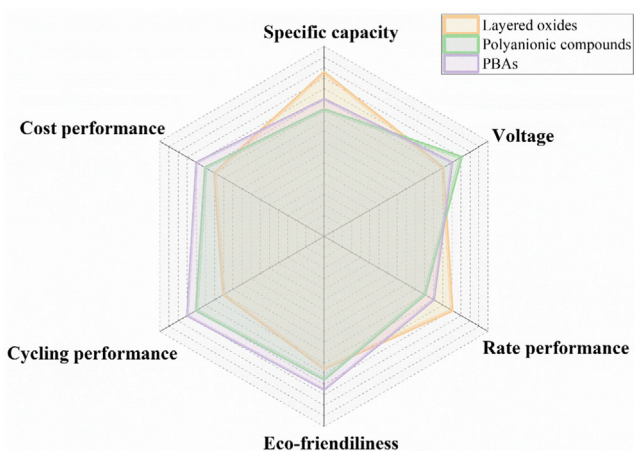


Figure 16. Comprehensive comparison of layered oxide, polyanionic material, and PBAs in aspect of commercialization.

expensive costs, structure instability, and adverse impacts on the environment. In contrast, polyanionic materials and PBAs exhibit a less polluted impact on the environment, which are more suitable for large-scale production, whereas lack specific capacity. Notably, Mn- and Fe-based cathode materials are worth exploring for their abundant resources and excellent electrochemical properties. Further exploration of these materials can lead to advancements in SIBs.

7. Conclusion

An ideal cathode material is supposed to possess the characteristics of: 1) high specific capacity; 2) high structure stability; 3) high thermal and chemical stability; 4) high cutoff voltage; 5) facile ion transfer kinetics; and 6) easy to obtain, low cost, and environment friendly. In this review, three eligible candidate cathode materials for SIBs are comprehensively introduced: layered oxides, polyanionic materials, and PBAs. Each material is analyzed in terms of structure characteristics, existing issues, recent achievements, progress, and environmental impacts. For layered oxides, the key challenges are insufficient specific, irreversible phase transition, and air sensitivity. To overcome these challenges, various strategies have been explored including element doping (cation dopant and anion dopant), surface coating (carbon, metal oxide, and organics), and structure architecture. Thereinto, cation doping is considered of great importance for it not only stabilizes the structure but also can activate anionic redox reaction, significantly enhancing specific capacity. Polyanionic materials attract worldwide researchers' interest for their virtue of high structure stability, even under extreme environmental conditions. However, poor electron conductivity limits their commercialization. A summary of enhanced strategies in recent years is introduced in this review, including element doping to enlarge Na⁺ diffusion channels, carbon coating, and compositing to enhance the electron conductivity, and morphology modification focusing on controlling the particle size and Na⁺ diffusion distance. In terms of PBAs, PBAs become popular because of one-step synthesis and low cost,

while the excess coordinated and interstitial water makes them less competitive. To address this issue, utmost efforts are supposed to be made to produce PBAs with low crystal water and vacancies. Among the optimization strategies, modifying the synthetic methods plays an effective role in eliminating excess water, for instance, through dehydration treatment. Overall, when it comes to practical commercialization, there is still a way for SIB cathode materials, more efforts should be devoted to making full-cell SIBs qualified for industrialization.

Despite the challenges, the rapid development of SIB cathode materials is promising. With continued advancements in material engineering, synthesis methods, and understanding of battery mechanisms, it is anticipated that layered oxides, polyanionic compounds, and PBAs will contribute significantly to the realization of large-scale energy storage systems.

Acknowledgements

This work was supported by the National Key Research and Development Program of China (grant no. 2022YFB2502000), the National Natural Science Foundation of China (grant no. U21A2033251771076), Guangdong Basic and Applied Basic Research Foundation (grant nos. 2020B1515120049, 2021A1515010332 and 2021A1515010153), and R&D Program in Key Areas of Guangdong Province (grant no. 2020B0101030005).

Conflict of Interest

The authors declare no conflict of interest.

Keywords

cathodes, layered oxides, optimization strategies, polyanionic compounds, Prussian Blue analogs, sodium-ion batteries

Received: April 29, 2023

Revised: June 2, 2023

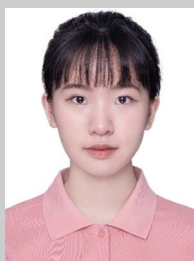
Published online:

- [1] Y. Chisti, *Biotechnol. Adv.* **2007**, *25*, 294.
- [2] S. Chu, A. Majumdar, *Nature* **2012**, *488*, 294.
- [3] A. Sharma, V. V. Tyagi, C. R. Chen, D. Buddhi, *Renewable Sustainable Energy Rev.* **2009**, *13*, 318.
- [4] L. Schlapbach, A. Zettler, *Nature* **2001**, *414*, 353.
- [5] This is indexed news from Angew. Chem, reported without indicating authors, *Angew. Chem. Int. Ed.* **2019**, *58*, 16723.
- [6] L. Xue, W. Zhou, S. Xin, H. Gao, Y. Li, A. Zhou, J. B. Goodenough, *Angew. Chem. Int. Ed.* **2018**, *57*, 14184.
- [7] N. S. Grundish, C. D. Amos, A. Agrawal, H. Khani, J. B. Goodenough, *Adv. Funct. Mater.* **2019**, *29*, 1903550.
- [8] Z. Dong, R. Zhang, D. Ji, N. A. Chernova, K. Karki, S. Sallis, L. Piper, M. S. Whittingham, *Adv. Sci.* **2016**, *3*, 1500229.
- [9] J. Ding, Y.-C. Lin, J. Liu, J. Rana, H. Zhang, H. Zhou, I.-H. Chu, K. M. Wiaderek, F. Omenya, N. A. Chernova, K. W. Chapman, L. F. J. Piper, S. P. Ong, M. S. Whittingham, *Adv. Energy Mater.* **2018**, *8*, 1800221.
- [10] A. Yoshino, *Angew. Chem. Int. Ed.* **2012**, *51*, 5798.
- [11] J. Liu, X. Xu, R. Hu, L. Yang, M. Zhu, *Adv. Energy Mater.* **2016**, *6*, 1600256.
- [12] J. Liu, D. Xue, *Adv. Mater.* **2008**, *20*, 2622.
- [13] X. Xu, J. Liu, J. Liu, L. Ouyang, R. Hu, H. Wang, L. Yang, M. Zhu, *Adv. Funct. Mater.* **2018**, *28*, 1707573.
- [14] J. Liu, P. Kopold, P. A. van Aken, J. Maier, Y. Yu, *Angew. Chem. Int. Ed.* **2015**, *54*, 9632.
- [15] J. Deng, C. Bae, A. Denlinger, T. Miller, *Joule* **2020**, *4*, 511.
- [16] R. Usiskin, Y. Lu, J. Popovic, M. Law, P. Balaya, Y.-S. Hu, J. Maier, *Nat. Rev. Mater.* **2021**, *6*, 1020.
- [17] This is editorial news from Nat. Energy, reported without indicating authors, *Nat. Energy* **2022**, *7*, 461.
- [18] N. Yabuuchi, K. Kubota, M. Dahbi, S. Komaba, *Chem. Rev.* **2014**, *114*, 11636.
- [19] C. Delmas, *Adv. Energy Mater.* **2018**, *8*, 1703137.
- [20] A. Mauger, C. M. Julien, J. B. Goodenough, K. Zaghib, *J. Electrochem. Soc.* **2019**, *167*, 070507.
- [21] C. Delmas, D. Carlier, M. Guignard, *Adv. Energy Mater.* **2021**, *11*, 2001201.
- [22] Y. Tian, Y. An, C. Wei, B. Xi, S. Xiong, J. Feng, Y. Qian, *Adv. Energy Mater.* **2021**, *11*, 2002529.
- [23] J. Liu, P. Kopold, C. Wu, P. A. van Aken, J. Maier, Y. Yu, *Energy Environ. Sci.* **2015**, *8*, 3531.
- [24] P. Barpanda, L. Lander, S. Nishimura, A. Yamada, *Adv. Energy Mater.* **2018**, *8*, 1703055.
- [25] Q. Liu, Z. Hu, M. Chen, Q. Gu, Y. Dou, Z. Sun, S. Chou, S. X. Dou, *ACS Appl. Mater. Interfaces* **2017**, *9*, 3644.
- [26] C. Delmas, J. Braconnier, A. Maazaz, P. Hagenmuller, *Rev. Chim. Miner.* **1982**, *19*, 343.
- [27] C. Zhao, Q. Wang, Z. Yao, J. Wang, B. Sánchez-Lengeling, F. Ding, X. Qi, Y. Lu, X. Bai, B. Li, H. Li, A. Aspuru-Guzik, X. Huang, C. Delmas, M. Wagemaker, L. Chen, Y.-S. Hu, *Science* **2020**, *370*, 708.
- [28] P.-F. Wang, Y. You, Y.-X. Yin, Y.-G. Guo, *Adv. Energy Mater.* **2018**, *8*, 1701912.
- [29] X. Li, Y. Wang, D. Wu, L. Liu, S.-H. Bo, G. Ceder, *Chem. Mater.* **2016**, *28*, 6575.
- [30] Q. Liu, Z. Hu, M. Chen, C. Zou, H. Jin, S. Wang, S. Chou, S. Dou, *Small* **2019**, *15*, 1805381.
- [31] Y. Zhao, Q. Liu, X. Zhao, D. Mu, G. Tan, L. Li, R. Chen, F. Wu, *Mater. Today* **2023**, *62*, 271.
- [32] R. Zhang, S. Yang, H. Li, T. Zhai, H. Li, *InfoMat* **2022**, *4*, e12305.
- [33] T. Wang, D. Su, D. Shanmukaraj, T. Rojo, M. Armand, G. Wang, *Electrochem. Energy Rev.* **2018**, *1*, 200.
- [34] T. Jin, H. Li, K. Zhu, P.-F. Wang, P. Liu, L. Jiao, *Chem. Soc. Rev.* **2020**, *49*, 2342.
- [35] L. Zhu, L. Li, J. Wen, Y.-R. Zeng, *J. Power Sources* **2019**, *438*, 227016.
- [36] P. Moreau, D. Guyomard, J. Gaubicher, F. Boucher, *Chem. Mater.* **2010**, *22*, 4126.
- [37] M. Avdeev, Z. Mohamed, C. D. Ling, J. Lu, M. Tamaru, A. Yamada, P. Barpanda, *Inorg. Chem.* **2013**, *52*, 8685.
- [38] Y. Zhu, Y. Xu, Y. Liu, C. Luo, C. Wang, *Nanoscale* **2012**, *5*, 780.
- [39] T. Boyadzhieva, V. Koleva, R. Stoyanova, *Phys. Chem. Chem. Phys.* **2017**, *19*, 12730.
- [40] J.-Z. Guo, H.-X. Zhang, Z.-Y. Gu, M. Du, H.-Y. Lü, X.-X. Zhao, J.-L. Yang, W.-H. Li, S. Kang, W. Zou, X.-L. Wu, *Adv. Funct. Mater.* **2022**, *32*, 2209482.
- [41] H. Gao, Y. Li, K. Park, J. B. Goodenough, *Chem. Mater.* **2016**, *28*, 6553.
- [42] Y. Yu, *Sodium-Ion Batteries: Energy Storage Materials and Technologies*, Wiley, Hefei, Anhui Province, China **2022**.
- [43] W. Yang, Q. Liu, Y. Zhao, D. Mu, G. Tan, H. Gao, L. Li, R. Chen, F. Wu, *Small Methods* **2022**, *6*, 2200555.

- [44] H. Kim, R. A. Shakoor, C. Park, S. Y. Lim, J.-S. Kim, Y. N. Jo, W. Cho, K. Miyasaka, R. Kahraman, Y. Jung, J. W. Choi, *Adv. Funct. Mater.* **2013**, *23*, 1147.
- [45] W. Song, Z. Wu, J. Chen, Q. Lan, Y. Zhu, Y. Yang, C. Pan, H. Hou, M. Jing, X. Ji, *Electrochim. Acta* **2014**, *146*, 142.
- [46] L. Sharma, R. Gond, B. Senthilkumar, A. Roy, P. Barpanda, *ACS Catal.* **2020**, *10*, 43.
- [47] M. Chen, D. Cortie, Z. Hu, H. Jin, S. Wang, Q. Gu, W. Hua, E. Wang, W. Lai, L. Chen, S.-L. Chou, X.-L. Wang, S.-X. Dou, *Adv. Energy Mater.* **2018**, *8*, 1800944.
- [48] W. Guan, B. Pan, P. Zhou, J. Mi, D. Zhang, J. Xu, Y. Jiang, *ACS Appl. Mater. Interfaces* **2017**, *9*, 22369.
- [49] Y. You, A. Manthiram, *Adv. Energy Mater.* **2018**, *8*, 1701785.
- [50] Q. Ni, Y. Bai, F. Wu, C. Wu, *Adv. Sci.* **2017**, *4*, 1600275.
- [51] D. Bin, Y. Du, B. Yang, H. Lu, Y. Liu, Y. Xia, *Adv. Funct. Mater.* **2023**, *33*, 2211765.
- [52] E. Goikolea, V. Palomares, S. Wang, I. R. Larramendi, X. Guo, G. Wang, T. Rojo, *Adv. Energy Mater.* **2020**, *10*, 2002055.
- [53] A. Paolella, C. Faure, V. Timoshhevskii, S. Marras, G. Bertoni, A. Guerfi, A. Vrijh, M. Armand, K. Zaghib, *J. Mater. Chem. A* **2017**, *5*, 18919.
- [54] J. Peng, W. Zhang, Q. Liu, J. Wang, S. Chou, H. Liu, S. Dou, *Adv. Mater.* **2022**, *34*, 2108384.
- [55] W.-J. Li, C. Han, G. Cheng, S.-L. Chou, H.-K. Liu, S.-X. Dou, *Small* **2019**, *15*, 1900470.
- [56] Y. You, X.-L. Wu, Y.-X. Yin, Y.-G. Guo, *Energy Environ. Sci.* **2014**, *7*, 1643.
- [57] J. Qian, C. Wu, Y. Cao, Z. Ma, Y. Huang, X. Ai, H. Yang, *Adv Energy Mater* **2018**, *8*, 1702619.
- [58] L. Jiang, Y. Lu, C. Zhao, L. Liu, J. Zhang, Q. Zhang, X. Shen, J. Zhao, X. Yu, H. Li, X. Huang, L. Chen, Y.-S. Hu, *Nat. Energy* **2019**, *4*, 495.
- [59] J. Peng, J. Wang, H. Yi, W. Hu, Y. Yu, J. Yin, Y. Shen, Y. Liu, J. Luo, Y. Xu, P. Wei, Y. Li, Y. Jin, Y. Ding, L. Miao, J. Jiang, J. Han, Y. Huang, *Adv. Energy Mater.* **2018**, *8*, 1702856.
- [60] W. Wang, Y. Gang, Z. Hu, Z. Yan, W. Li, Y. Li, Q.-F. Gu, Z. Wang, S.-L. Chou, H.-K. Liu, S.-X. Dou, *Nat. Commun.* **2020**, *11*, 980.
- [61] M. Ware, *J. Chem. Educ.* **2008**, *85*, 612.
- [62] J. Peng, M. Ou, H. Yi, X. Sun, Y. Zhang, B. Zhang, Y. Ding, F. Wang, S. Gu, C. A. López, W. Zhang, Y. Liu, J. Fang, P. Wei, Y. Li, L. Miao, J. Jiang, C. Fang, Q. Li, M. T. Fernández-Díaz, J. A. Alonso, S. Chou, J. Han, *Energy Environ. Sci.* **2021**, *14*, 3130.
- [63] H.-W. Lee, R. Y. Wang, M. Pasta, S. Woo Lee, N. Liu, Y. Cui, *Nat. Commun.* **2014**, *5*, 5280.
- [64] Y. Fang, X.-Y. Yu, X. W. Lou, *Angew. Chem. Int. Ed.* **2017**, *56*, 5801.
- [65] H. Niwa, T. Shibata, Y. Imai, S. Kimura, Y. Moritomo, *Batteries* **2017**, *3*, 5.
- [66] T. Shibata, Y. Fukuzumi, W. Kobayashi, Y. Moritomo, *Sci. Rep.* **2015**, *5*, 9006.
- [67] D. Tanabe, T. Shimono, W. Kobayashi, Y. Moritomo, *Phys. Status Solidi Rapid Res. Lett.* **2014**, *8*, 287.
- [68] L. Liang, X. Sun, D. K. Denis, J. Zhang, L. Hou, Y. Liu, C. Yuan, *ACS Appl. Mater. Interfaces* **2019**, *11*, 4037.
- [69] M.-H. Cao, Z. Shadike, S.-M. Bak, T. Wang, E. Hu, S. Ehrlich, Y.-N. Zhou, X.-Q. Yang, Z.-W. Fu, *Energy Storage Mater.* **2020**, *24*, 417.
- [70] S. Wang, F. Chen, X.-D. He, L.-M. Zhang, F. Chen, J.-R. Wang, J.-M. Dong, C.-H. Chen, *ACS Appl. Mater. Interfaces* **2021**, *13*, 12203.
- [71] J. Xu, Z. Han, K. Jiang, P. Bai, Y. Liang, X. Zhang, P. Wang, S. Guo, H. Zhou, *Small* **2020**, *16*, 1904388.
- [72] T. Shimono, D. Tanabe, W. Kobayashi, Y. Moritomo, *J. Phys. Soc. Jpn.* **2013**, *82*, 083601.
- [73] A. Kulka, C. Marino, K. Walczak, C. Borca, C. Bolli, P. Novak, C. Villevieille, *J. Mater. Chem. A* **2020**, *8*, 6022.
- [74] J. Zhang, H. Yuan, Y. Huang, S. Kan, Y. Wu, M. Bu, Y. Liu, P. He, H. Liu, *Chem. Eng. J.* **2021**, *417*, 128097.
- [75] E. Lee, D. E. Brown, E. E. Alp, Y. Ren, J. Lu, J.-J. Woo, C. S. Johnson, *Chem. Mater.* **2015**, *27*, 6755.
- [76] L. Durai, A. Gopalakrishnan, S. Badhulika, *Mater. Lett.* **2020**, *270*, 127739.
- [77] L. Sun, Y. Xie, X.-Z. Liao, H. Wang, G. Tan, Z. Chen, Y. Ren, J. Gim, W. Tang, Y.-S. He, K. Amine, Z.-F. Ma, *Small* **2018**, *14*, 1704523.
- [78] J.-J. Braconnier, C. Delmas, C. Fouassier, P. Hagenmuller, *Mater. Res. Bull.* **1980**, *15*, 1797.
- [79] Q. Zhao, F. K. Butt, Z. Guo, L. Wang, Y. Zhu, X. Xu, X. Ma, C. Cao, *Chem. Eng. J.* **2021**, *403*, 126308.
- [80] L. Yang, S. Luo, Y. Wang, Y. Zhan, Q. Wang, Y. Zhang, X. Liu, W. Mu, F. Teng, *Chem. Eng. J.* **2021**, *404*, 126578.
- [81] C. Cheng, M. Ding, T. Yan, J. Jiang, J. Mao, X. Feng, T. Chan, N. Li, L. Zhang, *Small Methods* **2022**, *6*, 2101524.
- [82] F. Zhang, J. Liao, L. Xu, W. Wu, X. Wu, *ACS Appl. Mater. Interfaces* **2021**, *13*, 40695.
- [83] R. Dang, Q. Li, M. Chen, Z. Hu, X. Xiao, *Phys. Chem. Chem. Phys.* **2018**, *21*, 314.
- [84] G. Wan, B. Peng, L. Zhao, F. Wang, L. Yu, R. Liu, G. Zhang, *SusMat* **2023**, *1*, 14.
- [85] H. Hu, H.-C. He, R.-K. Xie, C. Cheng, T. Yan, C. Chen, D. Sun, T.-S. Chan, J. Wu, L. Zhang, *Nano Energy* **2022**, *99*, 107390.
- [86] X. Cui, S. Wang, X. Ye, X. Fan, C. Gao, Y. Quan, S. Wen, X. Cai, J. Huang, S. Li, *Energy Storage Mater.* **2022**, *45*, 1153.
- [87] Q. Wang, Z. Shadike, X. Li, J. Bao, Q. Qiu, E. Hu, S. Bak, X. Xiao, L. Ma, X. Wu, X. Yang, Y. Zhou, *Adv. Energy Mater.* **2021**, *11*, 2003455.
- [88] G. Assat, J.-M. Tarascon, *Nat. Energy* **2018**, *3*, 373.
- [89] J. Jin, Y. Liu, X. Pang, Y. Wang, X. Xing, J. Chen, *Sci. China Chem.* **2021**, *64*, 385.
- [90] H. Xu, S. Guo, H. Zhou, *J. Mater. Chem. A* **2019**, *7*, 23662.
- [91] X. Zhang, Y. Qiao, S. Guo, K. Jiang, S. Xu, H. Xu, P. Wang, P. He, H. Zhou, *Adv. Mater.* **2019**, *31*, 1807770.
- [92] W. Zheng, Q. Liu, Z. Wang, Z. Wu, S. Gu, L. Cao, K. Zhang, J. Fransaer, Z. Lu, *Energy Storage Mater.* **2020**, *28*, 300.
- [93] H. Ren, Y. Li, Q. Ni, Y. Bai, H. Zhao, C. Wu, *Adv. Mater.* **2022**, *34*, 2106171.
- [94] A. Konarov, H. J. Kim, J.-H. Jo, N. Voronina, Y. Lee, Z. Bakenov, J. Kim, S.-T. Myung, *Adv. Energy Mater.* **2020**, *10*, 2001111.
- [95] A. J. Perez, D. Batuk, M. Saubanère, G. Rousse, D. Foix, E. McCalla, E. J. Berg, R. Dugas, K. H. W. van den Bos, M.-L. Doublet, D. Gonbeau, A. M. Abakumov, G. Van Tendeloo, J.-M. Tarascon, *Chem. Mater.* **2016**, *28*, 8278.
- [96] Z. Chen, M. Yang, Z. Huang, Y. Fu, Z. Chen, S. Li, M. Zhan, R. Wang, M. Chu, R. Qi, X. Cheng, Z. Ma, G. Chen, T. Zhang, J. Zhai, S. Xu, M. Zhang, J. Wang, W. Ji, S. Li, F. Pan, W. Yin, Y. Xiao, *Chem. Eng. J.* **2023**, *454*, 140396.
- [97] C. Chen, W. Huang, Y. Li, M. Zhang, K. Nie, J. Wang, W. Zhao, R. Qi, C. Zuo, Z. Li, H. Yi, F. Pan, *Nano Energy* **2021**, *90*, 106504.
- [98] L. Yu, Z. Cheng, K. Xu, Y.-X. Chang, Y.-H. Feng, D. Si, M. Liu, P.-F. Wang, S. Xu, *Energy Storage Mater.* **2022**, *50*, 730.
- [99] K. Wang, Z.-G. Wu, G. Melinte, Z.-G. Yang, A. Sarkar, W. Hua, X. Mu, Z.-W. Yin, J.-T. Li, X.-D. Guo, B.-H. Zhong, C. Kübel, *J. Mater. Chem. A* **2021**, *9*, 13151.
- [100] N. Jiang, Q. Liu, J. Wang, W. Yang, W. Ma, L. Zhang, Z. Peng, Z. Zhang, *Small* **2021**, *17*, 2007103.
- [101] J. Lamb, A. Manthiram, *ACS Appl. Energy Mater.* **2021**, *4*, 11735.
- [102] K. Wu, N. Li, K. Hao, W. Yin, M. Wang, G. Jia, Y. L. Lee, R. Dang, X. Deng, X. Xiao, E. Zhao, Z. Wu, *J. Phys. Chem. C* **2021**, *125*, 20171.
- [103] C.-Y. Yu, J.-S. Park, H.-G. Jung, K.-Y. Chung, D. Aurbach, Y.-K. Sun, S.-T. Myung, *Energy Environ. Sci.* **2015**, *8*, 2019.
- [104] J.-Y. Hwang, S.-T. Myung, J. U. Choi, C. S. Yoon, H. Yashiro, Y.-K. Sun, *J. Mater. Chem. A* **2017**, *5*, 23671.

- [105] Y. Li, Q. Shi, X. Yin, J. Wang, J. Wang, Y. Zhao, J. Zhang, *Chem. Eng. J.* **2020**, *402*, 126181.
- [106] Q. Deng, F. Zheng, W. Zhong, Q. Pan, Y. Liu, Y. Li, Y. Li, J. Hu, C. Yang, M. Liu, *Chem. Eng. J.* **2021**, *404*, 126446.
- [107] T. Or, S. W. D. Gourley, K. Kaliyappan, Y. Zheng, M. Li, Z. Chen, *Electrochim. Energy Rev.* **2022**, *5*, 20.
- [108] Y. Zhuang, J. Zhao, Y. Zhao, X. Zhu, H. Xia, *Sustain. Mater. Technol.* **2021**, *28*, e00258.
- [109] J. Xia, W. Wu, K. Fang, X. Wu, *Carbon* **2020**, *157*, 693.
- [110] J. Li, H. Hu, J. Wang, Y. Xiao, *Carbon Neutralization* **2022**, *1*, 96.
- [111] I. Moeez, D. Susanto, G. Ali, H.-G. Jung, H.-D. Lim, K. Y. Chung, *J. Mater. Chem. A* **2020**, *8*, 13964.
- [112] I. Moeez, D. Susanto, W. Chang, H.-D. Lim, K. Y. Chung, *Chem. Eng. J.* **2021**, *425*, 130547.
- [113] L. Tao, P. Sittisomwong, B. Ma, A. Hu, D. Xia, S. Hwang, H. Huang, P. Bai, F. Lin, *Energy Storage Mater.* **2023**, *55*, 826.
- [114] J. Wang, Y. Teng, G. Su, S. Bao, J. Lu, *J. Colloid Interface Sci.* **2022**, *608*, 2013.
- [115] J. Jiao, K. Wu, R. Dang, N. Li, X. Deng, X. Liu, Z. Hu, X. Xiao, *Electrochim. Acta* **2021**, *384*, 138362.
- [116] C.-H. Jo, J.-H. Jo, H. Yashiro, S.-J. Kim, Y.-K. Sun, S.-T. Myung, *Adv. Energy Mater.* **2018**, *8*, 1702942.
- [117] Y. Yu, W. Kong, Q. Li, D. Ning, G. Schuck, G. Schumacher, C. Su, X. Liu, *ACS Appl. Energy Mater.* **2020**, *3*, 933.
- [118] C. Chen, Z. Han, S. Chen, S. Qi, X. Lan, C. Zhang, L. Chen, P. Wang, W. Wei, *ACS Appl. Mater. Interfaces* **2020**, *12*, 7144.
- [119] C. Shi, L. Wang, X. Chen, J. Li, S. Wang, J. Wang, H. Jin, *Nanoscale Horiz.* **2022**, *7*, 338.
- [120] X. Xiang, K. Zhang, J. Chen, *Adv. Mater.* **2015**, *27*, 5343.
- [121] Y. Xiao, Y.-F. Zhu, H.-R. Yao, P.-F. Wang, X.-D. Zhang, H. Li, X. Yang, L. Gu, Y.-C. Li, T. Wang, Y.-X. Yin, X.-D. Guo, B.-H. Zhong, Y.-G. Guo, *Adv. Energy Mater.* **2019**, *9*, 1803978.
- [122] X. Xu, S. Ji, R. Gao, J. Liu, *RSC Adv.* **2015**, *5*, 51454.
- [123] X. Wang, X. Yin, X. Feng, Y. Li, X. Dong, Q. Shi, Y. Zhao, J. Zhang, *Chem. Eng. J.* **2022**, *428*, 130990.
- [124] Q. Shen, X. Zhao, Y. Liu, Y. Li, J. Zhang, N. Zhang, C. Yang, J. Chen, *Adv. Sci.* **2020**, *7*, 2002199.
- [125] J. Liang, Z. Li, J. Cheng, J. Qin, H. Liu, D. Wang, *Nano Res.* **2022**, *16*, 4987.
- [126] Q. Mao, R. Gao, Q. Li, D. Ning, D. Zhou, G. Schuck, G. Schumacher, Y. Hao, X. Liu, *Chem. Eng. J.* **2020**, *382*, 122978.
- [127] M. Chen, Q. Liu, S.-W. Wang, E. Wang, X. Guo, S.-L. Chou, *Adv. Energy Mater.* **2019**, *9*, 1803609.
- [128] L. N. Zhao, T. Zhang, H. L. Zhao, Y. L. Hou, *Mater. Today Nano* **2020**, *10*, 100072.
- [129] Y. Gao, H. Zhang, X.-H. Liu, Z. Yang, X.-X. He, L. Li, Y. Qiao, S.-L. Chou, *Adv. Energy Mater.* **2021**, *11*, 2101751.
- [130] L. Xiao, F. Ji, J. Zhang, X. Chen, Y. Fang, *Small* **2023**, *19*, 2205732.
- [131] S. Chen, C. Wu, L. Shen, C. Zhu, Y. Huang, K. Xi, J. Maier, Y. Yu, *Adv. Mater.* **2017**, *29*, 1700431.
- [132] Q. Zheng, H. Yi, X. Li, H. Zhang, *J. Energy Chem.* **2018**, *27*, 1597.
- [133] H. Kim, H. Lim, H.-S. Kim, K. J. Kim, D. Byun, W. Choi, *Nano Res.* **2019**, *12*, 397.
- [134] M. Peng, D. Zhang, L. Zheng, X. Wang, Y. Lin, D. Xia, Y. Sun, G. Guo, *Nano Energy* **2017**, *31*, 64.
- [135] S. Xu, Y. Yang, F. Tang, Y. Yao, X. Lv, L. Liu, C. Xu, Y. Feng, X. Rui, Y. Yu, *Mater. Horiz.* **2023**, *10*, 1901.
- [136] X. Liu, G. Feng, E. Wang, H. Chen, Z. Wu, W. Xiang, Y. Zhong, Y. Chen, X. Guo, B. Zhong, *ACS Appl. Mater. Interfaces* **2019**, *11*, 12421.
- [137] H. Yu, X. Ruan, J. Wang, Z. Gu, Q. Liang, J.-M. Cao, J. Kang, C.-F. Du, X.-L. Wu, *ACS Nano* **2022**, *16*, 21174.
- [138] R. Chen, D. S. Butenko, S. Li, D. Li, X. Zhang, J. Cao, I. V. Ogorodnyk, N. I. Klyui, W. Han, I. V. Zatovsky, *J. Mater. Chem. A* **2021**, *9*, 17380.
- [139] Q.-Y. Zhao, J.-Y. Li, M.-J. Chen, H. Wang, Y.-T. Xu, X.-F. Wang, X. Ma, Q. Wu, X. Wu, X.-X. Zeng, *Nano Lett.* **2022**, *22*, 9685.
- [140] C. Guo, J. Yang, Z. Cui, S. Qi, Q. Peng, W. Sun, L.-P. Lv, Y. Xu, Y. Wang, S. Chen, *J. Energy Chem.* **2022**, *65*, 514.
- [141] Z.-Y. Gu, J.-Z. Guo, J.-M. Cao, X.-T. Wang, X.-X. Zhao, X.-Y. Zheng, W.-H. Li, Z.-H. Sun, H.-J. Liang, X.-L. Wu, *Adv. Mater.* **2022**, *34*, 2110108.
- [142] F. Xiong, J. Li, C. Zuo, X. Zhang, S. Tan, Y. Jiang, Q. An, P. K. Chu, L. Mai, *Adv. Funct. Mater.* **2023**, *33*, 2211257.
- [143] X. Liu, L. Tang, Z. Li, J. Zhang, Q. Xu, H. Liu, Y. Wang, Y. Xia, Y. Cao, X. Ai, *J. Mater. Chem. A* **2019**, *7*, 18940.
- [144] J. Wang, J. Kang, Z.-Y. Gu, Q. Liang, X. Zhao, X. Wang, R. Guo, H. Yu, C.-F. Du, X.-L. Wu, *Adv. Funct. Mater.* **2022**, *32*, 2109694.
- [145] Q. Deng, Q. Cheng, X. Liu, C. Chen, Q. Huang, J. Li, W. Zhong, Y. Li, J. Hu, H. Wang, L. Wu, C. Yang, *Chem. Eng. J.* **2022**, *430*, 132710.
- [146] Z. Hu, R. Zhang, C. Fan, X. Liu, P. Gao, W. Zhang, Z. Liu, S. Han, J. Liu, J. Liu, *Small* **2022**, *18*, 2201719.
- [147] M. J. Aragón, P. Lavela, G. F. Ortiz, R. Alcántara, J. L. Tirado, *ChemElectroChem* **2018**, *5*, 367.
- [148] Y. Cao, X.-L. Li, X. Dong, M. Liao, N. Wang, J. Cheng, J. Xu, Y. Qi, Y. Liu, Y. Xia, *Small* **2022**, *18*, 2204830.
- [149] W. Shen, H. Li, Z. Guo, C. Wang, Z. Li, Q. Xu, H. Liu, Y. Wang, Y. Xia, *ACS Appl. Mater. Interfaces* **2016**, *8*, 15341.
- [150] P. Hu, T. Zhu, C. Cai, B. Mai, C. Yang, J. Ma, L. Zhou, H. J. Fan, L. Mai, *Adv. Funct. Mater.* **2022**, *32*, 2208051.
- [151] W. Li, M. Li, K. R. Adair, X. Sun, Y. Yu, *J. Mater. Chem. A* **2017**, *5*, 13882.
- [152] R. Klee, M. J. Aragón, P. Lavela, R. Alcántara, J. L. Tirado, *ACS Appl. Mater. Interfaces* **2016**, *8*, 23151.
- [153] J. Gao, Y. Tian, Y. Mei, L. Ni, H. Wang, H. Liu, W. Deng, G. Zou, H. Hou, X. Ji, *Chem. Eng. J.* **2023**, *458*, 141385.
- [154] J. Hu, J. Zhang, H. Li, Y. Chen, C. Wang, *J. Power Sources* **2017**, *351*, 192.
- [155] F. Li, Y.-E. Zhu, J. Sheng, L. Yang, Y. Zhang, Z. Zhou, *J. Mater. Chem. A* **2017**, *5*, 25276.
- [156] H. Ma, J. Bai, P. Wang, W. Li, Y. Mao, K. Xiao, X. Zhu, B. Zhao, Y. Sun, *Adv. Mater. Interfaces* **2022**, *9*, 2201386.
- [157] B. Pandit, M. T. Sougrati, B. Fraisse, L. Monconduit, *Nano Energy* **2022**, *95*, 107010.
- [158] K. Wang, X. Huang, T. Zhou, D. Sun, H. Wang, Z. Zhang, *J. Mater. Chem. A* **2022**, *10*, 10625.
- [159] M. Su, J. Shi, Q. Kang, D. Lai, Q. Lu, F. Gao, *Chem. Eng. J.* **2022**, *432*, 134289.
- [160] W. Li, Z. Yao, Y. Liu, S. Zhang, X. Wang, X. Xia, C. Gu, J. Tu, *Chem. Eng. J.* **2022**, *433*, 133557.
- [161] J. Liu, Y. Zhao, X. Huang, Y. Zhou, K. Lam, D. Y. W. Yu, X. Hou, *Chem. Eng. J.* **2022**, *435*, 134839.
- [162] Y. Geng, T. Zhang, T. Xu, W. Mao, D. Li, K. Dai, J. Zhang, G. Ai, *Energy Storage Mater.* **2022**, *49*, 67.
- [163] X. Shen, Q. Zhou, M. Han, X. Qi, B. Li, Q. Zhang, J. Zhao, C. Yang, H. Liu, Y.-S. Hu, *Nat. Commun.* **2021**, *12*, 2848.
- [164] W. Zhang, J. Lu, Z. Guo, *Mater. Today* **2021**, *50*, 400.
- [165] Y. Zhou, Y. Yang, M. Jiao, Z. Zhou, *Sci. Bull.* **2018**, *63*, 146.
- [166] H. Song, K. Eom, *Adv. Funct. Mater.* **2020**, *30*, 2003086.
- [167] Y. Qi, Z. Tong, J. Zhao, L. Ma, T. Wu, H. Liu, C. Yang, J. Lu, Y.-S. Hu, *Joule* **2018**, *2*, 2348.
- [168] J. He, T. Tao, F. Yang, Z. Sun, *ACS Appl. Mater. Interfaces* **2021**, *13*, 60099.
- [169] W. Wang, Y. Gang, J. Peng, Z. Hu, Z. Yan, W. Lai, Y. Zhu, D. Appadoo, M. Ye, Y. Cao, Q.-F. Gu, H.-K. Liu, S.-X. Dou, S.-L. Chou, *Adv. Funct. Mater.* **2022**, *32*, 2111727.

- [170] X.-H. Liu, J. Peng, W.-H. Lai, Y. Gao, H. Zhang, L. Li, Y. Qiao, S.-L. Chou, *Adv. Funct. Mater.* **2022**, *32*, 2108616.
- [171] A. Zhou, W. Cheng, W. Wang, Q. Zhao, J. Xie, W. Zhang, H. Gao, L. Xue, J. Li, *Adv. Energy Mater.* **2021**, *11*, 2000943.
- [172] L. Ma, H. Cui, S. Chen, X. Li, B. Dong, C. Zhi, *Nano Energy* **2021**, *81*, 105632.
- [173] X. Liu, Y. Cao, J. Sun, *Adv. Energy Mater.* **2022**, *12*, 2202532.
- [174] Y. Xu, M. Ou, Y. Liu, J. Xu, X. Sun, C. Fang, Q. Li, J. Han, Y. Huang, *Nano Energy* **2020**, *67*, 104250.
- [175] Y. Zhou, Y. Jiang, Y. Zhang, Y. Chen, Z. Wang, A. Liu, Z. Lv, M. Xie, *ACS Appl. Mater. Interfaces* **2022**, *14*, 32149.
- [176] H. Zhang, J. Peng, L. Li, Y. Zhao, Y. Gao, J. Wang, Y. Cao, S. Dou, S. Chou, *Adv. Funct. Mater.* **2023**, *33*, 2210725.
- [177] J. Peng, B. Zhang, W. Hua, Y. Liang, W. Zhang, Y. Du, G. Peleckis, S. Idris, Q. Gu, Z. Cheng, J. Wang, H. Liu, S. Dou, S. Chou, *Angew. Chem. Int. Ed.* **2023**, *62*, e202215865.
- [178] C. Zhao, Z. Yao, D. Zhou, L. Jiang, J. Wang, V. Murzin, Y. Lu, X. Bai, A. Aspuru-Guzik, L. Chen, Y.-S. Hu, *Adv. Funct. Mater.* **2020**, *30*, 1910840.
- [179] S. Phadke, R. Mysyk, M. Anouti, *J. Energy Chem.* **2020**, *40*, 31.
- [180] C. Ling, J. Chen, F. Mizuno, *J. Phys. Chem. C* **2013**, *117*, 21158.
- [181] C. Xu, Y. Ma, J. Zhao, P. Zhang, Z. Chen, C. Yang, H. Liu, Y.-S. Hu, *Angew. Chem. Int. Ed.* **2023**, *62*, e202217761.
- [182] M. Ye, S. You, J. Xiong, Y. Yang, Y. Zhang, C. C. Li, *Mater. Today Energy* **2022**, *23*, 100898.
- [183] Y. You, H.-R. Yao, S. Xin, Y.-X. Yin, T.-T. Zuo, C.-P. Yang, Y.-G. Guo, Y. Cui, L.-J. Wan, J. B. Goodenough, *Adv. Mater.* **2016**, *28*, 7243.
- [184] S. J. R. Prabakar, J. Jeong, M. Pyo, *RSC Adv.* **2015**, *5*, 37545.
- [185] Y. Qiao, G. Wei, J. Cui, M. Zhang, X. Cheng, D. He, S. Li, Y. Liu, *Chem. Commun.* **2019**, *55*, 549.
- [186] W.-J. Li, S.-L. Chou, J.-Z. Wang, J.-L. Wang, Q.-F. Gu, H.-K. Liu, S.-X. Dou, *Nano Energy* **2015**, *13*, 200.
- [187] Y. Liu, D. He, Y. Cheng, L. Li, Z. Lu, R. Liang, Y. Fan, Y. Qiao, S. Chou, *Small* **2020**, *16*, 1906946.
- [188] Q. Zhang, L. Fu, J. Luan, X. Huang, Y. Tang, H. Xie, H. Wang, *J. Power Sources* **2018**, *395*, 305.
- [189] Y. Huang, M. Xie, Z. Wang, Y. Jiang, Y. Yao, S. Li, Z. Li, L. Li, F. Wu, R. Chen, *Small* **2018**, *14*, 1801246.
- [190] F. Feng, S. Chen, X.-Z. Liao, Z.-F. Ma, *Small Methods* **2019**, *3*, 1800259.
- [191] P. Wan, H. Xie, N. Zhang, S. Zhu, C. Wang, Z. Yu, W. Chu, L. Song, S. Wei, *Adv. Funct. Mater.* **2020**, *30*, 2002624.
- [192] Z. Wang, Y. Huang, D. Chu, C. Li, Y. Zhang, F. Wu, L. Li, M. Xie, J. Huang, R. Chen, *ACS Appl. Mater. Interfaces* **2021**, *13*, 38202.
- [193] M. Morant-Giner, R. Sanchis-Gual, J. Romero, A. Alberola, L. Garcia-Cruz, S. Agouram, M. Galbiati, N. M. Padial, J. C. Waerenborgh, C. Martí-Gastaldo, S. Tatay, A. Forment-Aliaga, E. Coronado, *Adv. Funct. Mater.* **2018**, *28*, 1706125.
- [194] Z. Li, L. Zhang, X. Ge, C. Li, S. Dong, C. Wang, L. Yin, *Nano Energy* **2017**, *32*, 494.
- [195] D. Zuo, C. Wang, J. Han, J. Wu, H. Qiu, Q. Zhang, Y. Lu, Y. Lin, X. Liu, *ACS Sustainable Chem. Eng.* **2020**, *8*, 16229.
- [196] X. Li, Y. Shang, D. Yan, L. Guo, S. Huang, H. Y. Yang, *ACS Nano* **2022**, *16*, 453.
- [197] J. Peng, Y. Gao, H. Zhang, Z. Liu, W. Zhang, L. Li, Y. Qiao, W. Yang, J. Wang, S. Dou, S. Chou, *Angew. Chem. Int. Ed.* **2022**, *61*, e202205867.
- [198] C.-M. Xu, J. Peng, X.-H. Liu, W.-H. Lai, X.-X. He, Z. Yang, J.-Z. Wang, Y. Qiao, L. Li, S.-L. Chou, *Small Methods* **2022**, *6*, 2200404.
- [199] T. Huang, Y. Niu, Q. Yang, W. Yang, M. Xu, *ACS Appl. Mater. Interfaces* **2021**, *13*, 37187.
- [200] J. Guo, F. Feng, S. Zhao, Z. Shi, R. Wang, M. Yang, F. Chen, S. Chen, Z.-F. Ma, T. Liu, *Carbon Energy* **2023**, *5*, e314.
- [201] L. Shen, Y. Jiang, Y. Jiang, J. Ma, K. Yang, H. Ma, Q. Liu, N. Zhu, *ACS Appl. Mater. Interfaces* **2022**, *14*, 24332.
- [202] M. Baumann, M. Häringer, M. Schmidt, L. Schneider, J. F. Peters, W. Bauer, J. R. Binder, M. Weil, *Adv. Energy Mater.* **2022**, *12*, 2202636.
- [203] C. Sun, S. Li, M. Bai, W. Wu, X. Tang, W. Zhao, M. Zhang, Y. Ma, *Energy Storage Mater.* **2020**, *27*, 252.
- [204] D. Yuan, X. Hu, J. Qian, F. Pei, F. Wu, R. Mao, X. Ai, H. Yang, Y. Cao, *Electrochim. Acta* **2014**, *116*, 300.
- [205] Q. Liu, Z. Hu, M. Chen, C. Zou, H. Jin, S. Wang, S. Chou, Y. Liu, S. Dou, *Adv. Funct. Mater.* **2020**, *30*, 1909530.



Chenxi Peng obtained her bachelor's degree in material science and engineering from Northwestern Polytechnical University in 2022. She is now a master student studying at South China University of Technology under the supervision of Prof. Jun Liu. Her research interests are the layered oxide cathodes for sodium-ion batteries.



Xijun Xu received his Ph.D. degree from South China University of Technology in 2019. From 2020 to 2021, he worked as a visiting fellowship at City University of Hongkong for electrocatalytic CO₂ reduction. He currently works in the College of Chemical Engineering and Light Industry at Guangdong University of Technology, P.R. China. Dr. Xu has been focused on designing nanostructured transition metal compounds as cathode/anode materials for Li/Na/K-ion batteries. Currently, his research interest includes nanoarray-based flexible electrodes, metal–organic framework derived materials, and solid-state polymer electrolytes for alkali-ion batteries.



Jun Liu is a professor of materials science and engineering at South China University of Technology, P.R. China. He received his Ph.D. in chemical engineering from Dalian University of Technology in 2010. From 2012 to 2015, he worked as a postdoctoral researcher at Deakin University and Max-Planck-Institute for Solid State Research. His current research interests mainly include the design of novel electrodes and electrolytes for rechargeable batteries, especially for Li-/Na-ion, Li–S, and all-solid-state batteries.